DESIGN OF III-V MULTIJUNCTION SOLAR CELLS ON SILICON SUBSTRATE

Nikhil Jain

Thesis submitted to the faculty of the Virginia Polytechnic Institute and State University in partial fulfillment of the requirements for the degree of

Master of Science
In
Electrical Engineering

Mantu K. Hudait

Mariusz K. Orlowski

Kathleen Meehan

May 6, 2013
Blacksburg, VA

Keywords: Solar Cells, Multijunction, III-V Semiconductors, Solar Cell Modeling

DESIGN OF III-V MULTIJUNCTION SOLAR CELLS ON SILICON SUBSTRATE

Nikhil Jain

ABSTRACT

With looming energy crisis across the globe, achieving high efficiency and low cost solar cells have long been the key objective for photovoltaic researchers. III-V compound semiconductor based multijunction solar cells have been the dominant choice for space power due to their superior performance compared to any other existing solar cell technologies. In spite of unmatched performance of III-V solar cells, Si cells have dominated the terrestrial market due to their lower cost. Most of the current III-V solar cells are grown on Ge or GaAs substrates, which are not only smaller in diameter, but are also more expensive than Si substrate. Direct integration of high efficiency III-V solar cells on larger diameter, cheaper and readily available Si substrate is highly desirable for increased density, low-cost and lightweight photovoltaics. However, the polar-on-nonpolar epitaxy, the thermal mismatch and the 4% lattice mismatch makes the direct growth of GaAs on Si challenging, rendering the metamorphic cell sensitive to dislocations.

The focus of this work is to investigate and correlate the impact of threading dislocation density on the performance of lattice-mismatched single-junction (1J) GaAs and dual-junction (2J) InGaP/GaAs solar cells on Si substrate. Utilizing our calibrated dislocation-assisted modeling process, we present the design methodology to optimize the structure of 2J InGaP/GaAs solar cell on Si substrate. Our modeling results suggest an optimistic future for integrating III-V solar cell technology on Si substrate and will be useful for future design and prediction of metamorphic III-V solar cell performance on Si substrate.

Dedicated to my grandparents,

Ratan Bhushan and Usha Jain,

Jagdish and Rani Jain

and my parents,

Saurabh and Monica Jain

ACKNOWLEDGEMENTS

I would like to sincerely thank and express my deepest gratitude to my adviser, Dr. Mantu Hudait for giving me the opportunity to work under his guidance. He's been extremely supportive and I'm grateful to him for his continued encouragement and faith in my ideas. I would also like to thank the members of my committee: Dr. Kathleen Meehan, Dr. Mariusz Orlowski and Dr. Masoud Agah for their guidance and support during my research work. A special thanks to Matthew Meitl and John Wilson at Semprius for being excellent mentors.

Being one of the first students at the ADSEL group has been challenging, but the learning has been extremely rewarding. My lab mates Yan Zhu and Siddharth Vijayaragahavn provided great company during MBE installation phase. I specially thank Yan for answering my never-ending list of questions related to MBE growth and for all the fun times at ADSEL. I would also like to thank the Crosslight team for all their help and support during this research.

I gratefully acknowledge the funding support from the Institute for Critical Technology and Applied Sciences, Virginia Tech. I would also like to thank all my teachers and friends who have supported me all through these years and helped me grow into a better individual. Lastly, I would like to extend my sincere thanks to my entire family for their unconditional support, love and encouragement. I thank my father, Saurabh Jain for being extremely supportive and for his guidance along every facet of life and my mother, Monica Jain for teaching me to be humble and content, but at the same be always hungry to seek improvement. A special thanks to my brother, Vinay Jain and his wife, Megha Jain for their love and support and for keeping the family knitted together. I am also very grateful to Apoorva for being my pillar of support & strength.

TABLE OF CONTENTS

LIST OF FIGURES

LIST OF TABLES

CHAPTER 1

INTRODUCTION

The ever increasing global energy demand and the depleting fossil fuel resources have motivated significant interest in research and development of renewable energy resources. Solar, wind and hydroelectric are among the most widely used renewable energy sources today. Even though contribution of renewable energy towards our current energy generation is insignificant, however, it is predicted that these new emerging technologies especially wind and solar will contribute substantially towards are future energy generation as can be seen in Figure 1.1 [1]. Solar energy is a clean and carbon-free energy resource with tremendous potential for electricity generation. Light emitted by the sun and falling on the earth is one of the most abundant energy resources. Over 15,000 EJ ($1.5x10^{22}$ J) of solar energy reaches earth every day, compared to daily energy consumption of approximately 1.3 EJ by human activity [2]. Thus, clean and the abundant amount of available solar energy resource makes it a very attractive for future energy generation. Efficient collection, storage and distribution of solar energy in cost-effective manners will be important to realize the maximum potential of solar energy for our future energy needs.

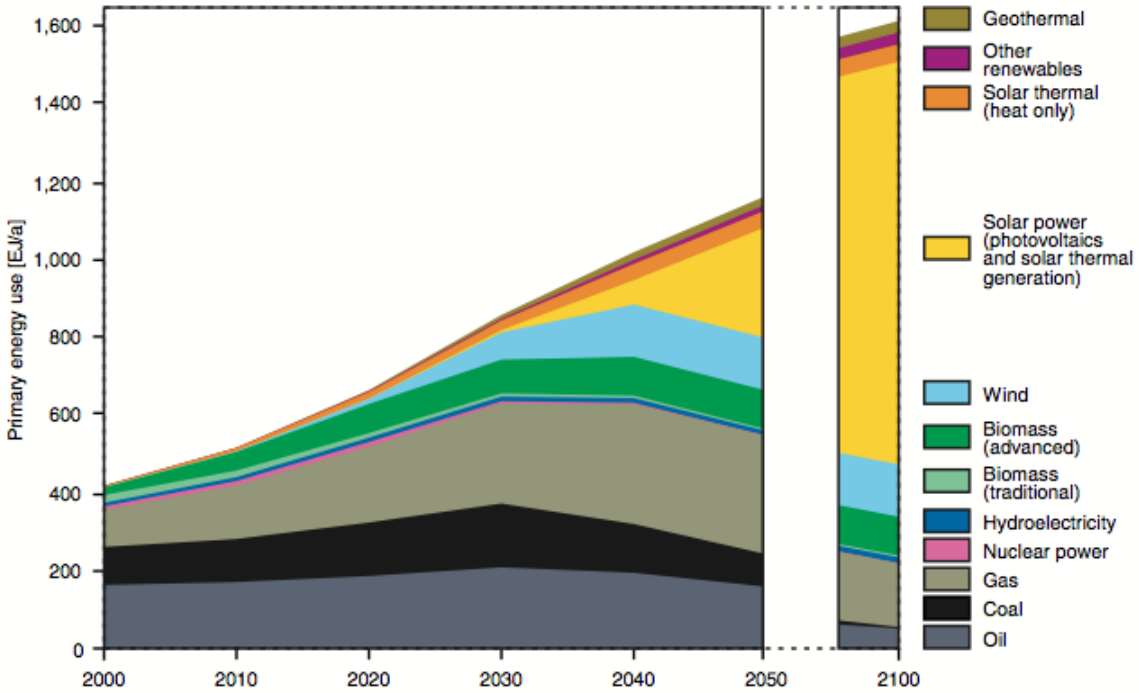

Figure 1.1 Transformation of global energy resources: from past into the future, Source: WBGU [1]. Used under fair use, 2013.

In this chapter, we will give a brief introduction about solar cells and their history. Classification of solar cells into various categories will be discussed and the progress in performance of the respective solar technologies will be summarized. Finally, the motivation for integrating compound semiconductor based high-efficiency III-V multijunction solar cells on low-cost, cheap and readily available Si substrate will be addressed.

1.1 Solar Cells

A solar cell is a device, which allows direct conversion of incident sunlight energy into electrical energy. Typically, the semiconductor absorbs incident photons with energy higher than the band-gap of the semiconductor. Semiconductor material solar cells are typically based on p-n junctions. Under illumination, these solar cells operate under forward bias, where the incident

light creates the bias. When photons are absorbed under illumination, electron-hole pairs are created. When a material absorbs light, photon lose their energy to excite the electrons to higher energy levels. The excited electrons slowly decay to their ground state. These excited electrons are extracted and fed into an external circuit before they can relax to their ground state. These generated carriers need to be efficiently collected to be able to contribute towards photocurrent and hence, electricity generation.

1.2 Brief History and Progress in Solar Cell Technology

Edmund Becquerel first demonstrated the photovoltaic effect in 1839. However, it was not until 1883 that the first solid-state solar cell was built by Charles Fritts by melting a thin sheet of selenium between gold as one of the metal contacts and another metal [3]. Russell Ohl used silicon for the first time for making solar cells in 1939 while he was working with silicon for point contact rectifiers [4]. The low efficiency of such cells limited their applications for terrestrial power generation. However, the immense interest among the Soviet scientists for solar cells led them to apply the technology to power the first space satellite, the *Sputnik* [5]. Motivated by their application in space power primarily due to their portability and a clean energy generation mechanism, researchers began to work on improving the performance of solar cells. The oil crisis of the 1970's began to draw attention to find alternative energy sources, which started the modern era of solar cells. Significant progress has been made towards the development of both space and terrestrial solar cells in the last few decades. Researchers have spent efforts to understand and develop the photovoltaic properties in various kinds of materials. Most common materials used for solar cell applications have been based on silicon, GaAs, CdTe, CIGS. Cells based on such materials have typical efficiencies in excess of 15%. Recently, organic solar cells have also gained attention. Dye-sensitized solar cells have reached an

efficiency of 11.4% [6], however, their low efficiency have not attracted much commercial use yet. Silicon and CdTe based solar cells have dominated the terrestrial solar cell market primarily due to their relatively lower cost, while the high-efficiency III-V compound semiconductor solar cells have dominated the space & satellite applications. However, their expensive cost has limited their application for terrestrial sector. III-V compound semiconductor based triple-junction solar cells currently hold the world record efficiency of 44% under concentrated sunlight of 947 suns [6]. The progress made by various solar technologies in the last 35 to 40 years has been summarized in a single graph plotted by the Department of Energy's National Renewable Energy Laboratory as shown in Figure 1.2 [7].

1.3 Lattice-matched III-V Solar Cells

Unlike silicon, the III-V compound semiconductor materials provide the flexibility to realize

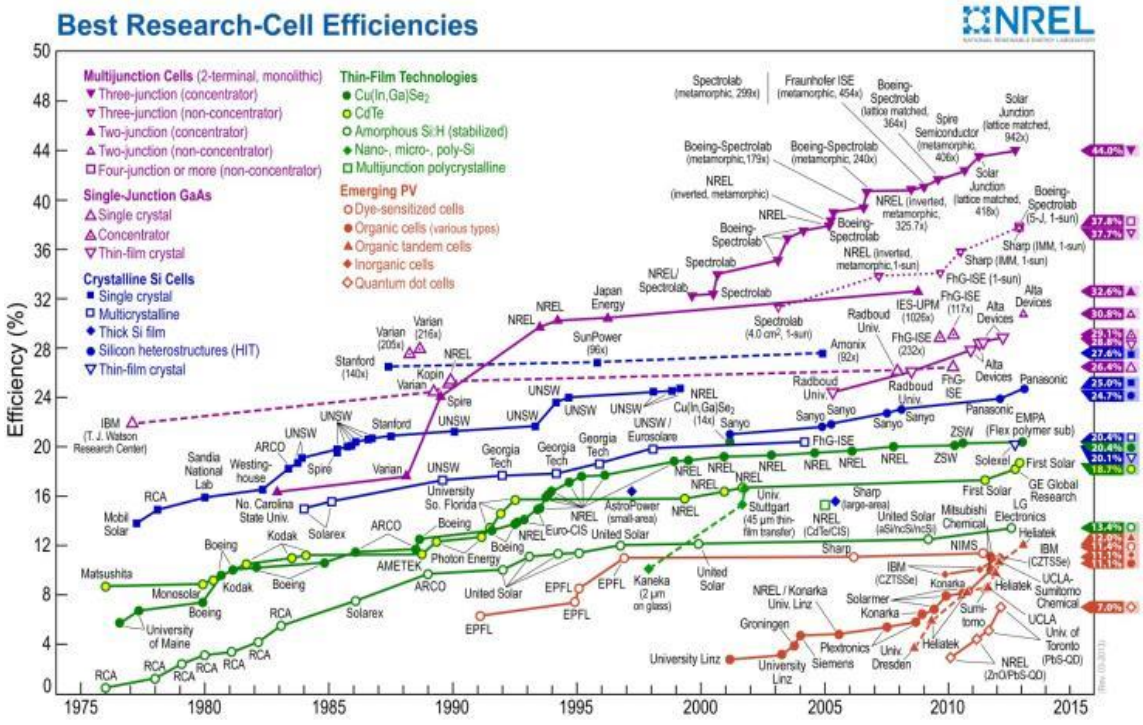

Figure 1.2 Progress in various solar cell technologies over the last 35-40 years [7]. Used under fair use, 2013.

multiple solar cells stacked on top of each other following same crystal lattice. The flexibility in band-gap selection provides an unprecedented degree of freedom in solar cell design through metamorphic or lattice-matched configurations based on III-V materials. From the Figure 1.3 [8], we can clearly see that the multiple solar cells stacked on top of one another in III-V multijunction solar cells allow a much broader absorption of the incident solar spectrum compared to the conventional single-junction (1J) Si solar cells. The multiple III-V solar cells when connected in series and designed in such a way that they generate the same photo-current, allows linear addition of the voltages from the individual subcell resulting in higher conversion efficiencies. Figure 1.4 shows the band-gap vs. lattice constant and gives an overview of different compound semiconductor alloys that can be made by careful engineering the band-gaps and lattice constants in a device design. The four most readily available semiconductor substrates include Si, Ge, GaAs and InP. This places a constraint on the band-gap and lattice-constant selection for optimal device design, wherein lattice-match structure are desired. The horizontal green lines in Figure 1.4 indicate the ideal band-gap combination (1.85-1.90eV/ 1.42eV/ 1.0eV) for realizing high-efficiency triple-junction (3J) solar cell on GaAs substrate [9], [10]. The highest efficiency achieved from lattice-matched thin film 1J GaAs and 2J InGaP/GaAs solar cells are 28.8% and 30.8%, respectively at 1-sun [6]. A record efficiency of 32.6% at 1000 suns has been demonstrated for the 2J InGaP/GaAs cell on GaAs substrate [11]. However, experimental realization of high quality epitaxial 3J solar cells comprising of subcells with the ideal band-gap combinations has been quite challenging. Utilizing Ge (band-gap = 0.67eV) as the bottom subcell in a lattice-matched 3J solar cell configuration, cell efficiency in excess of 40% was demonstrated for the first time by King et al [2]. In search for 1eV bottom subcell, the most commonly followed path initially was the integration of 1eV metamorphic InGaAs solar

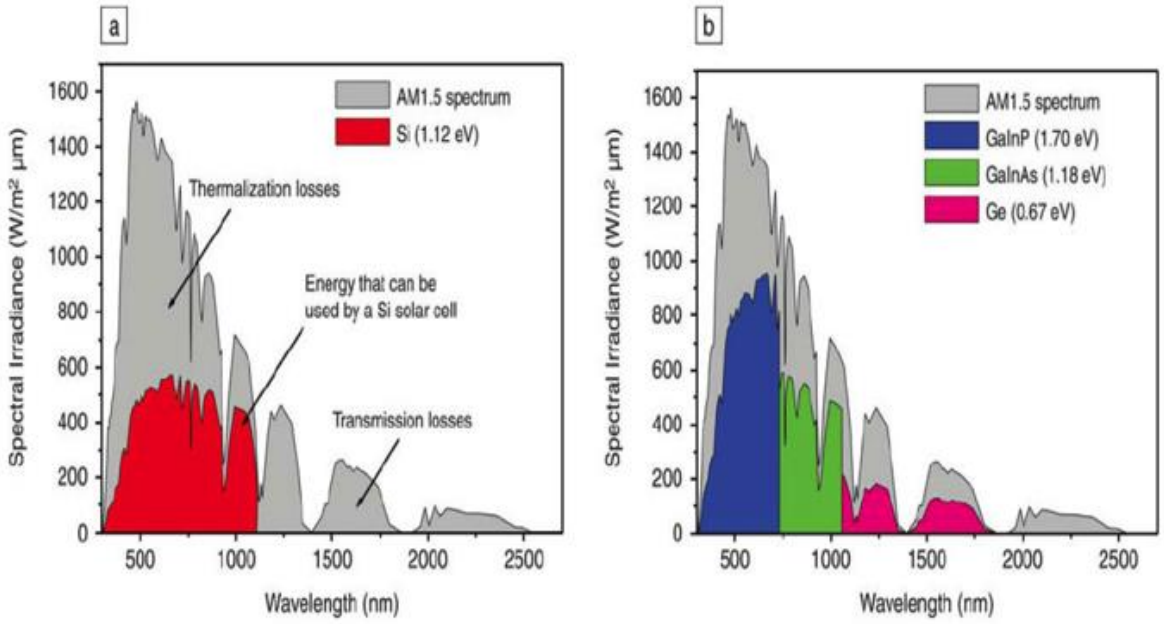

Figure 1.3 AM1.5 spectrum and the parts of the spectrum than can, in theory, be used by: (a) Si solar cells and (b) $Ga_{0.35}In_{0.65}P/Ga_{0.83}In_{0.17}As$/Ge solar cells [8]. Used under fair use, 2013.

cell in the 3J solar cell configuration with lattice-matched InGaP and GaAs as the top two subcells [12]. To gain additional performance benefits, the InGaAs cell was grown the last in an inverted configuration and this approach is commonly known as inverted metamorphic or IMM approach [12]. This IMM approach lead to an efficiency of 40.8% which utilized two metamorphic InGaAs subcells with band-gaps of 1.34eV and 0.89eV as the bottom two subcells in the 3J solar cell configuration.

With recent development in the dilute nitride based III-V materials, high quality 1eV InGaAsN alloys have been made possible by molecular beam epitaxy [13]. Dilute nitride based solar cells utilizing InGaP (1.9eV)/ GaAs (1.4eV)/ InGaAsN (1eV) cell architecture have reached world record efficiency of 44% under concentrated sunlight of 947 suns [6]. By stacking an infinite number of junctions, theoretical efficiency of 86% under maximum solar irradiance is achievable [14].

1.4 Motivation for III-V Solar Cells on Si Substrate

Direction integration of III-V compound semiconductors onto Si substrate has been of great interest for integrating the excellent optical and transport properties of III-V compound semiconductors with the volume manufacturability of Si. Successful integration of III-V on Si will benefit devices and related applications for RF & VLSI systems, optoelectronics, photonic integrated circuits and for optical interconnects to facilitate chip-to-chip communication.

Multijunction III-V solar cells have been the dominant choice for space satellite power primarily due to their high efficiencies. However, their expensive cost has limited their widespread commercialization for terrestrial applications. Most of the current III-V solar cells are either grown on GaAs or Ge substrate. Commercially available GaAs and Ge substrate are

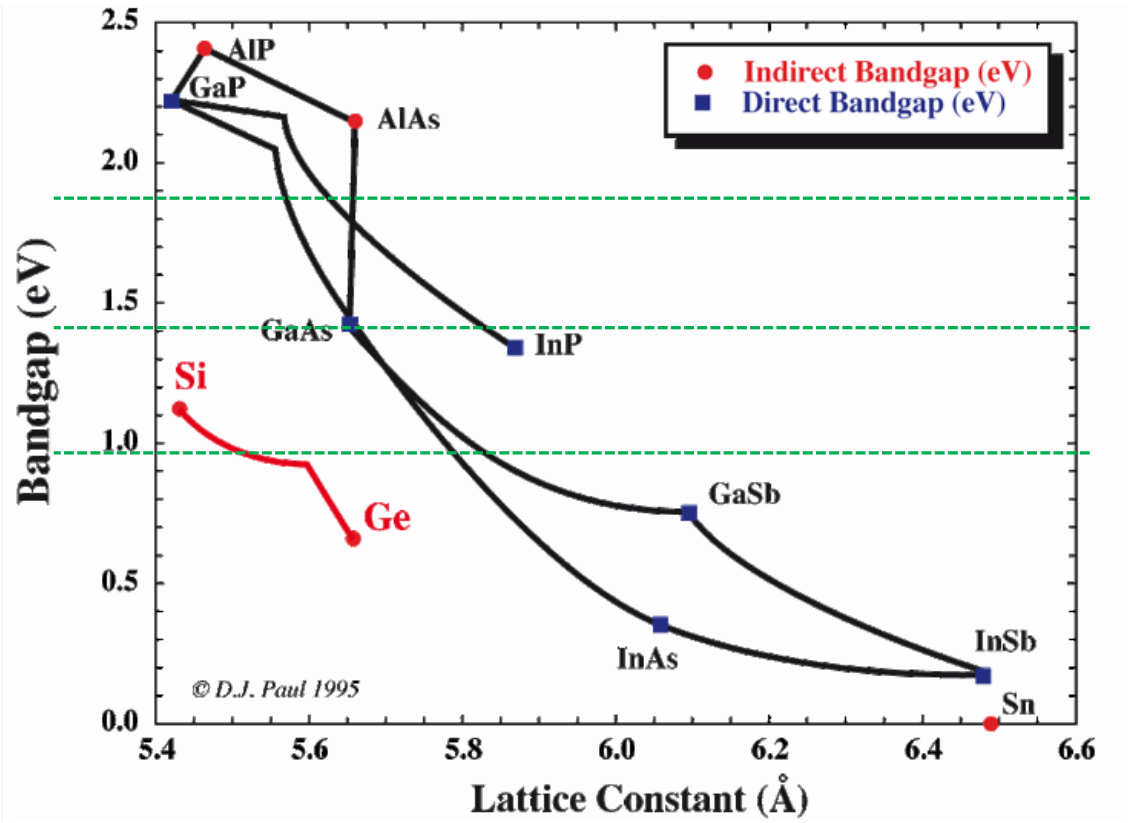

Figure 1.4 Semiconductor energy band gap versus crystal lattice constant. The horizontal lines represent the ideal band gap combination for triple-junction solar cells.

not only smaller in diameter compared to Si substrate, but are also much more expensive than Si. Direct integration of III-V compound semiconductors on large diameter, cheaper and readily available Si substrate is highly desirable for increased density, low-cost & lightweight photovoltaics. III-V integration on Si combines the excellent optical properties of compound semiconductors with the volume manufacturability of silicon allowing a path for significantly driving down the cell cost. III-V on Si technology is also attractive for integration with commercially available substrate re-use techniques for additional cost savings such as the spalling [15] and the epitaxial lift-off [16]-[18] techniques. Furthermore, the direct GaAs on Si epitaxy process can be extended and employed in conjunction with the current record efficient 3J solar cells utilizing dilute nitride bottom cell [6] and as well as with the current state-of-the-art IMM triple junction solar cell [12] production lines. Additionally, utilizing GaAs based solar cells on Si under higher concentration enables the cell to operate in a regime where the open-circuit voltage (V_{oc}) is dominated by the (n=1) diffusion current and not by the (n=2) recombination current due to the dislocations [19], allowing more favorable utilization of III-V solar cells on Si for concentrated photovoltaics applications. Four-junction mechanically stacked solar cells, incorporating a 4-terminal AlGaAs/GaAs-Si-InGaAs structure were shown to be the highest performing III-V/Si solar cells under the AM1.5D spectrum with an overall efficiency of 49% under 1-Sun illumination. This can be further increased to efficiency in excess of 55% under 500x sun concentration [20].

1.5 Challenges for Integrating III-V Solar Cells on Si

The viability of III-V InGaP/GaAs solar cells on Si relies on the ability to grow high quality GaAs on Si with careful lattice engineering and substrate treatment. The polar on non-polar epitaxy, the thermal mismatch and the 4% lattice-mismatch makes the growth of GaAs on Si

very challenging, rendering the metamorphic solar cell sensitive to defects including dislocation. These dislocations generated due to mismatch between GaAs and Si can propagate into the photoactive cell region and significantly impede the minority carrier lifetime and hence the overall cell performance [21]-[24].

The thermal expansion coefficient for Si and GaAs are - α(Si) = 2.6x10-6 K-1 and α(GaAs) = 5.7 x10-6 K-1 at 300 K, respectively. During GaAs growth on Si, cooling the sample from typical growth temperature of about ~600°C, the contribution of thermal mismatch strain is lower than the lattice mismatch strain. Hence, for modeling the impact of dislocations, the dislocations generated due to thermal mismatch can be ignored compared to the dislocations generated due to lattice mismatch.

The impact of threading dislocation density (TDD) on cell performance has been previously investigated [25]-[30]; however, their analysis was limited to only single-junction (1J) GaAs solar cell on Si substrate. The short-circuit current density (J_{sc}) used for modeling the impact of TDD on open-circuit voltage was assumed to be independent of TDD [29], which in reality decrease with increase in the dislocation density. There has not been significant work done on the modeling-assisted design of metamorphic tandem solar cells incorporating the impact of TDD. This thesis provides a comprehensive modeling and the optimization process for designing metamorphic 2J n^+/p InGaP/GaAs solar cell on Si under AM1.5G spectrum using finite element analysis without assuming a constant J_{sc}.

The highest efficiency reported for single-junction (1J) GaAs on Si is 21.3% at 200 suns under AM 1.5D spectrum [19]. While, the highest efficiency achieved for monolithic dual-junction 2J InGaP/GaAs solar cell on Si substrate is 18.6% at 1-sun under AM1.5G spectrum

[31]. The corresponding highest efficiency achieved from lattice-matched thin film 2J InGaP/GaAs cells is 30.8% at 1-sun [6]. This record efficient lattice-matched thin film 2J solar cell was grown on GaAs substrate, which was then epitaxially released from the GaAs substrate using a wet-etching process. The lower efficiency of the 2J InGaP/GaAs solar cell on Si substrate [31] could be attributed to thick Si_XGe_{1-X} buffer layer, insufficient optimization of anti-reflective layers and most likely inadequate realization of the current-matching condition between the subcells, taking into account the impact of threading dislocations [31]. Thus, it becomes extremely important to develop models for III-V solar cell design on Si substrate, which takes into account the threading dislocations, generated due to mismatch. Comprehensive dislocation-assisted modeling of metamorphic solar cells will help assess the tolerance of such defects on the device performance and improve their long-term reliability.

1.6 Research Objective

The main focus of this thesis is to investigate and optimize the performance of III-V InGaP/GaAs based dual-junction solar cells on Si substrate by taking into account the threading dislocations generated due to mismatch between GaAs and Si. The highest efficiency achieved till date utilizing the lattice-matched 2J InGaP/GaAs solar cells on GaAs substrate is 30.8% at 1-sun under AM1.5G spectrum [6]. Our goal is to investigate if one can theoretically model and optimize the performance of 2J InGaP/GaAs solar cell on Si substrate in close agreement with the performance of lattice-matched 2J InGaP/GaAs solar cells on GaAs substrate. This work probes the impact of dislocation in detail and asks questions like:

1. Can careful solar cell design enable III-V lattice-mismatched solar cells with similar performance compared to lattice-matched configuration?

2. How high dislocation density can the metamorphic solar cell tolerate without significant degradation in the performance?
3. In a multijunction solar cell design, which of the subcells is more sensitive to dislocations?
4. Due to dislocations, is the current density more impacted in a solar cell or the voltage?
5. What is the impact of surface recombination velocity in lattice-mismatched solar cells?

1.7 Organization of this Thesis

In Chapter 2, the physics and operation of solar cells is discussed along with the design fundamentals of III-V multijunction solar cells. The important solar cell characteristics are presented in Chapter 2. Chapter 3 describes our modeling approach based on finite element method. In Chapter 3, we describe the dislocation-dependent minority carrier lifetime model along with the important material and transport parameters subsequently utilized for solar cell modeling. Also the important assumptions during the modeling process are summarized. The last section of the Chapter 3 describes our model calibration with the state-of-the-art experimental solar cell results.

In Chapter 4, we provide a systematic study on the correlation of threading dislocation density and minority carrier lifetime on the 1J and 2J solar cell figure-of-merits, namely, efficiency (η), open-circuit voltage (V_{oc}), short-circuit current density (J_{sc}) and fill factor (FF). The next section in Chapter 4 presents our approach to engineer the metamorphic 2J InGaP/GaAs solar cell structure on Si to achieve the current-matching condition between each subcell at a TDD of 10^6 cm^{-2}. Finally, the impact of surface recombination on the cell performance is discussed. The results from our detailed cell modeling provide a quantitative assessment of solar cell figure-of-merits as a function of TDD. Chapter 5 concludes the thesis,

the results are summarized and the future work and scope of this research are presented. The modeling & design of the 2J InGaP/GaAs solar cell on Si presented in this work would be useful for future design & prediction of lattice-mismatched III-V multijunction solar cell performance on Si substrate.

CHAPTER 2

SOLAR CELL PHYSICS

2.1 Solar Spectrum

Nuclear fusion process, wherein helium is created from hydrogen, powers the sun. This process causes the temperature of the sun's core and the sun's surface to be 1.57×10^7 K and ~ 5578 K, respectively. The radiations from the sun coming at such high temperatures can be approximated as blackbody radiations. The solar spectrum and the corresponding solar intensity reaching the earth's surface are different than the spectrum reaching the outer space. The air mass coefficients (AM) have been defined for comparing the solar module performance under

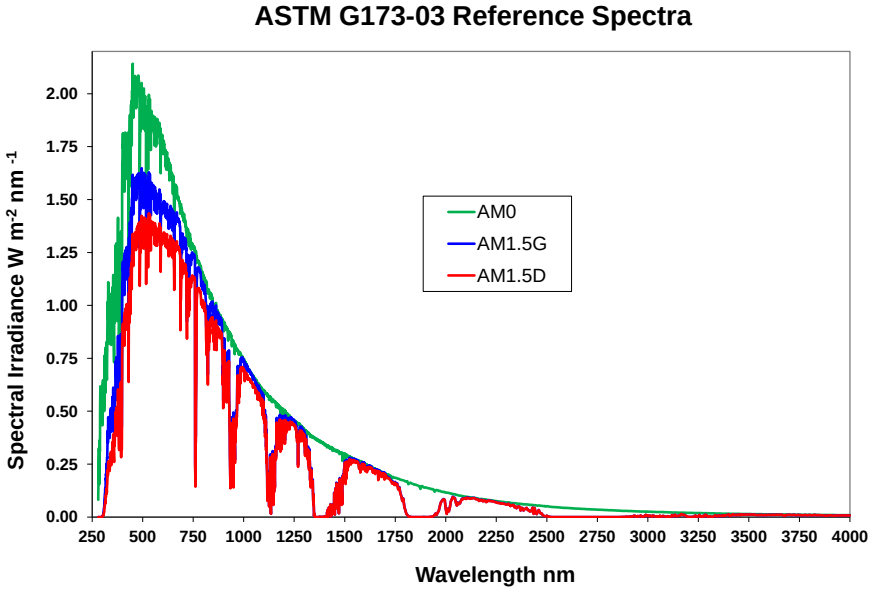

Figure 2.1 Solar Spectrums for AM0, AM1.5G and AM1.5D [1]. Used under fair use, 2013.

standard test conditions. Air mass helps define the length of the path through the atmosphere the radiation would have to travel in relation to the shortest length if the sun was in the apex. For solar radiations incident at a zenith angle (z) relative to the normal to the earth's surface, the air mass coefficient can be defined as:

$$AM = \frac{1}{\cos(z)} \tag{2.1}$$

The standard air masses for space, terrestrial and concentrated sunlight are defined as AM0, AM1.5G (global) and AM1.5D (direct), respectively and the corresponding spectrums are shown in Figure 2.1 [1]. The corresponding incident intensities for AM0, AM1.5G and AM1.5D are

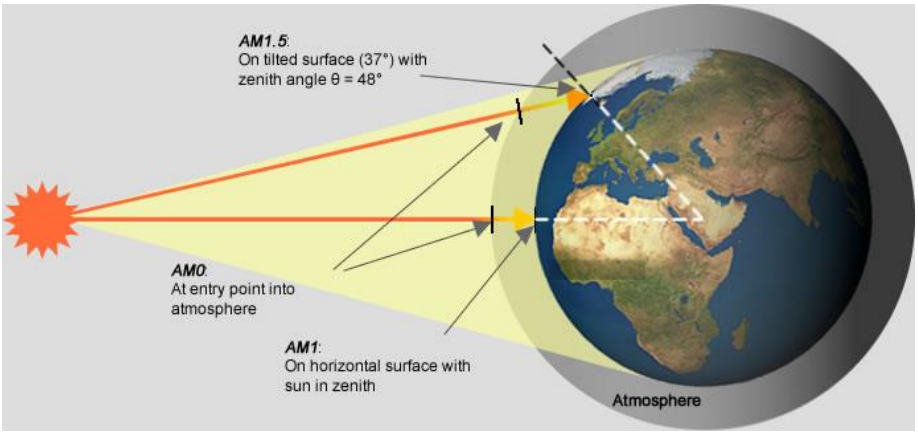

Figure 2.2 Illustration of various air mass (AM) positions and the zenith point [2]. Used under fair use, 2013.

~1356 W/m^2, ~1003 W/m^2 and ~887 W/m^2 respectively. Figure 2.2 representing the zenith angles for the different air mass solar spectrums [2].

The theoretically calculated efficiencies under AM1.5G and AM0 spectrums as a function of semiconductor band gap are shown in the Figure 2.3 [3]. The optimal band gaps for AM1.5G and AM0 are 1.4eV and 1.6eV respectively. These theoretical efficiencies ignore the losses due to

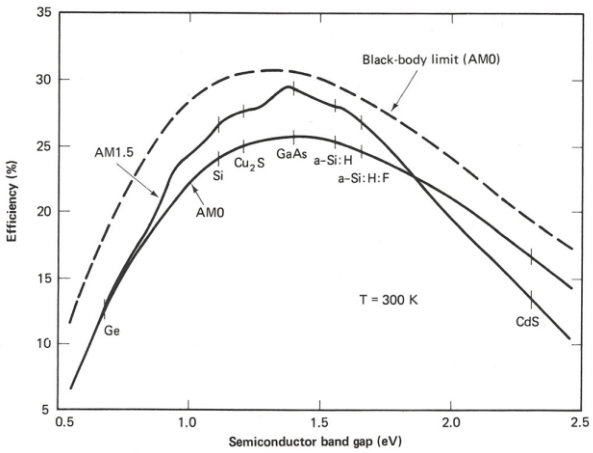

Figure 2.3 Efficiency vs. band gap for AM0 and AM1.5G spectrums [3]. Used under fair use, 2013.

surface recombination, absorption coefficients, limited cell thickness and the influence of material properties which relate to various recombination losses in a solar cell.

2.2 Solar Cell Device Structure

Creating p-n junctions region in semiconductors forms the most commonly used solar cells. Figure 2.4 shows a cross-sectional schematic of a typical n+/p homojunction solar cell. The layer that is illuminated first is called the emitter layer and is usually more heavily doped and thinner

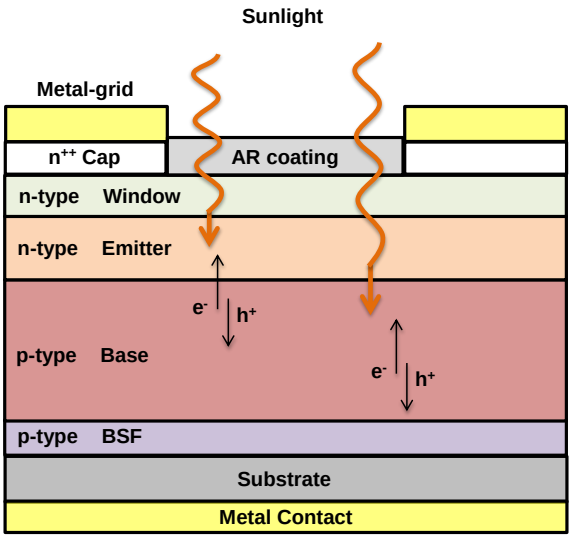

Figure 2.4 Cross-sectional schematic of a typical n+/p homojunction solar cell.

than the base layer. Most of the light absorption in a solar cell happens in the thicker and lightly doped base layer. Lower doping ensures higher minority carrier lifetime and higher diffusion coefficients, which in turn improves the carrier diffusion length. Furthermore, lower doping in the base increases the depletion region in the base, which can aid in carrier collection due to the electric field. However, too low doping may increase the dark current, which may significantly degrade the device performance.

The window and back surface field (BSF) are heterostructures, which are designed to reduce the recombination at the interfaces by passivation of the dangling bonds. Additionally, these heterostructures are selected with appropriate band-offsets to reflect the minority carriers. The window layer is designed to have a large valence band-offset to reflect the holes, while the BSF is designed to have a large conduction band-offset to reflect the electrons. These heterostructures are typically grown lattice matched to the cell and the semiconductor alloys used for these heterostructures are chosen to have higher band gap than the active junction material to minimize photon generation in these layers. The band-diagram for a typical n+/p 1J GaAs solar cell, which

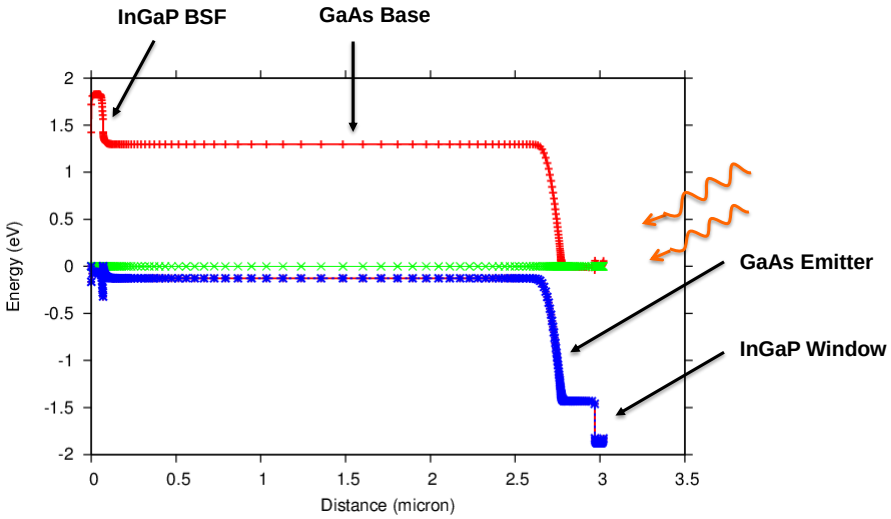

Figure 2.5 Band gap of 1J n+/p GaAs solar cell at equilibrium.

utilizes lattice-matched $In_{0.49}Ga_{0.51}P$ layer as both the window and the BSF layer, is shown in Figure 2.5. Besides these important III-V semiconductor layers, a solar cell consists of a back metal contact, front metal gridlines and an anti-reflective coating on the top surface (Figure 2.4).

A multijunction solar cell consists of multiple individual subcells that are stacked on top of each other to form a series connection. The individual subcells are connected to each other through tunnel junctions, which are designed to have very low series resistance primarily due to their high doping. These tunnel junctions are typically very thin to allow the tunneling mechanism to dominate the majority carrier transport. One of the most important design criteria in optimizing the performance of a multijunction solar cell is to achieve the current-matching condition between the subcells. Current-matching enables to extract the best performance from a multijunction solar cell by allowing linear addition of the open-circuit voltages from the respective subcells. The multijunction solar cells are typically current-matched by optimizing the doping and the thicknesses of various layers in each subcell. The subcell generating the least photocurrent limits the overall cell performance due to the series connection. The design of anti-reflective coating may also play an important role in realizing the current-matching condition between the subcells. An additional design parameter, which becomes extremely important for concentrated photovoltaic application is the front grid spacing optimization to minimize the losses due to grid shadowing and series resistance.

2.3 Solar Cell Device Operation

In a single-junction solar cell, incident photons with energies higher than the band-gap energy of the cell typically gets absorbed, while the photons with energies lower than the band-gap typically pass through the cell unabsorbed. When a photon is absorbed, it excites an electron

from the valence band to the conduction band, creating an electron-hole pair. These generated carriers diffuse through the quasi-neutral region until they reach the p-n junction where the drift mechanism begins to dominate the carrier transport due to the built-in electric field and sweeps away the carriers across the depletion region to become majority carriers. Electrons generated in the p-side travel towards the n-side and holes generated in the n-side travel towards the p-side. This redistribution of carriers sets up a potential difference, V_{oc} which is created due to the

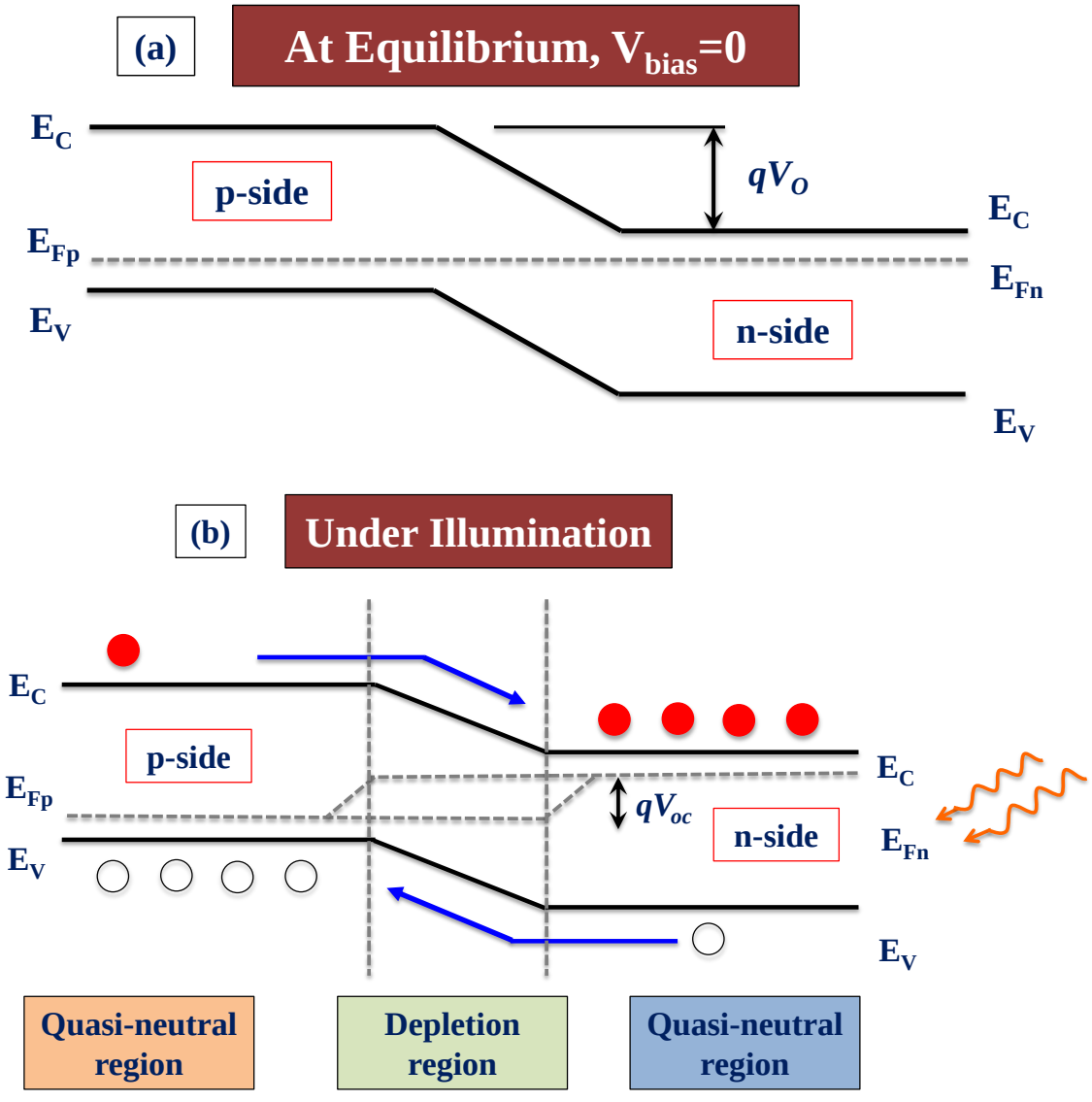

Figure 2.6 Band-diagrams representing solar cell operation (a) at equilibrium, and (b) under illumination.

splitting of the thermal equilibrium Ferm-level (E_F) into minority electron quasi-Fermi level (E_{Fn}), and minority hole quasi-Fermi level, E_{Fp}. This difference gives rise to the open-circuit voltage, $V_{oc} \approx (E_{Fn}-E_{Fp})/q$. This separation in the quasi-Fermi level is represented in the band-diagram shown in the Figure 2.6.

The electrons generated move towards the top cathode and the holes moves towards the bottom anode as shown in Figure 2.4. Under illumination, the electron-hole pair generation might not significantly increase the majority carrier concentration; however, the minority carrier concentration is significantly increased and hence, the diffusion current dominates due to the concentration gradient developed in the quasi-neutral region. The flow of generated minority carriers essentially defines the direction of the light induced current density or the photogenerated current density (J_{ph}) flowing from n-terminal to p-terminal. Collection of all the negative charges on the n-side and the positive charges on the p-side creates a light-induced forward bias to the solar cell. As a result of this forward bias in the presence of an external load, diode current begins to flow in the opposite direction to the photogenerated current and is typically referred as the diode dark current, $J_{dark.}$ It is important to minimize the dark current as it reduces the photogenerated current. Diode current measurements reveal important information about the recombination mechanism prevalent in the solar cell, which may limit its performance.

One of the most important solar cell material parameters is the minority carrier diffusion length (L_n *or* L_p), which depends on the minority carrier lifetime (τ_n *or* τ_p) and minority carrier diffusion coefficient (D_n *or* D_p). Their relationship is given by:

$$L = \sqrt{D\tau} \tag{2.2}$$

$$\frac{D}{\mu} = \frac{kT}{q} \tag{2.3}$$

These parameters are really important during the design of cell thicknesses and doping. The idea is to maximize the diffusion length to allow the minority carriers to reach their respective majority carrier side for collection to the external circuit. The cell thicknesses are designed in accordance with the minority carrier diffusion lengths. These parameters are dependent on the doping concentration.

2.4 Characteristics of Solar Cells

For a solar cell under illumination, from the simple diode equation, the output current (*J*) can be expressed as:

$$J = J_0 \left(e \frac{qV}{nkT} - 1 \right) - J_{\text{ph}} \tag{2.4}$$

where *J* is the current density, *V* is the voltage, J_{ph} is the photogenerated current density, J_0 is the diode saturation current density, *n* is the diode ideality factor, *k* is the Boltzmann's constant and *T* is the temperature. The first term on the right hand side of the equation represents the diode dark current (J_{dark}). The photogenerated current density J_{ph} is nearly equal to the short-circuit density, J_{sc} of a solar cell, to a good approximation. The current-voltage (IV) characteristic of a single-junction solar cell under illumination (red curve) and under no illumination (blue curve) are represented in Figure 2.7. Typically in good solar cells, the magnitude of the photogenerated current is significantly higher than the dark current. The diode reverse saturation current density maybe be contributed by the two mechanisms, n=1 and n=2 (n is the ideality factor). The ideal diode current (n=1) accounts for the recombination in the quasi-neutral region of the solar cell as

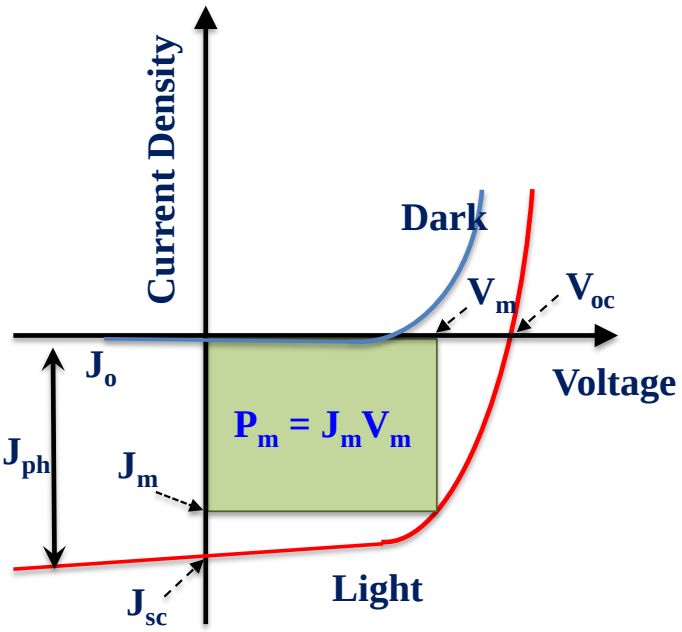

Figure 2.7 Current-voltage (IV) characteristic of a solar under illumination (red curve) and under no illumination or dark (blue curve).

well as for the finite dimensions of the cell and associated interface recombination, while the depletion region dark current (n=2) accounts for the carrier recombination in the depletion region of the solar cell. Thus, the overall dark current can be represented as follows:

$$J_{dark} = J_{01} e \left(\frac{qV}{n_1 kT} - 1\right) + J_{02} e \left(\frac{qV}{n_2 kT} - 1\right) \quad (2.5)$$

where the first term represents the ideal diffusion dark current density and the second term represents the depletion region recombination current density.

The quantum efficiency, *QE(E)* of a solar cell is defined as the probability of an incident photon to generate an electron-hole pair that can be collected as external photocurrent. The internal quantum efficiency, *IQE(E)* of the solar cell subtracts the reflectance component from the *QE(E)* and thus takes into account only the number of absorbed photons for extracting the quantum efficiency. The quantum efficiency of a cell depends on the material quality, absorption

coefficient and ability of the cell to efficiently separate and collect the carriers. The short-circuit current density, J_{sc} of a solar cell is related to the quantum efficiency, *QE(E)* as:

$$J_{sc} = q \int b_s\ (E).QE(E).dE \tag{2.6}$$

where q is the elementary charge and $b_s\,(E)$ is the incident photon flux density, i.e., the number of photons with energy in the range of E and $E+dE$ incident on a unit area per unit time.

Under illumination, the electron-hole pair generation might not significantly increase the majority carrier concentration; however, the minority carrier concentration significantly increases, causing the quasi-Fermi levels to split. This split in the quasi-Fermi levels creates the open-circuit voltage, V_{oc} that is defined at the maximum potential difference across the solar cell under open-circuit condition and can be expressed as:

$$V_{oc} = \frac{nkT}{q} ln\left(\frac{J_{sc}}{J_0} + 1\right) \tag{2.7}$$

The maximum power from the solar cell is obtained when the resistance of the load is selected such that it allows both the current and voltage to be maximized. This point at which this output power is maximized is called the maximum power point, P_m and can be expressed as:

$$P_m = J_m V_m \tag{2.8}$$

where J_m and V_m are the current density and voltage at the maximum power point, respectively. The shaded region in Figure 2.7 represents the maximum power point. The fill-factor (*FF*) is an important solar cell parameter which relates to measure of the quality or the "squareness" of the IV curve of a solar cell and can be expressed as:

$$FF = \frac{P_m}{J_{sc}V_{oc}} = \frac{J_m V_m}{J_{sc}V_{oc}} \tag{2.9}$$

The efficiency of a solar cell (η) describes its ability to efficiently convert incident photons into output electrical power. It can be defined as the amount of maximum power density delivered (P_m) as a fraction of the incident sunlight power density (P_{in}) and can be expressed as:

$$\eta = \frac{P_m}{P_{in}} = \frac{J_m V_m}{P_{in}} = \frac{FF\ J_{sc}V_{oc}}{P_{in}} \tag{2.10}$$

The equivalent circuit model of a solar cell with the series resistance (R_s) and shunt resistance (R_{sh}) element is shown in the Figure 2.8 and the total current density in a solar cell taking into account the influence of R_s and R_{sh} can be expressed as:

$$J = J_L - J_0(exp\left[\frac{V+JR_s}{nkT/q}\right] - \frac{V+JR_s}{R_{sh}}) \tag{2.11}$$

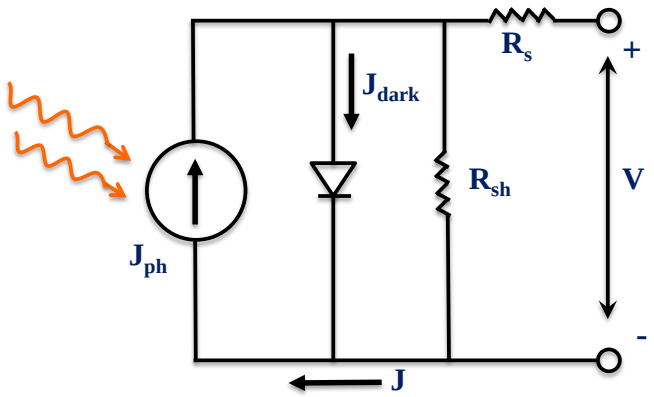

Figure 2.8 Equivalent circuit model of a solar cell under illumination.

CHAPTER 3

SOLAR CELL MODELING

3.1 Finite Element Method

Finite element analysis is one of the preferred modeling approach for solar cells as this method allows the flexibility to vary multiple parameters simultaneously, namely – lifetime, surface recombination velocities, band-gaps, anti-reflective coating design, material compositions, doping-type, doping concentration, layer thicknesses etc. This numerical simulation platform enables the investigation of individual parameters as well as coupled parameters in a much faster environment compared to analytical solutions.

The modeling process for optimizing our III-V multijunction solar cell designs was performed using the APSYS simulator, a general-purpose 2D/3D finite element analysis and modeling software for semiconductor devices [1]-[2]. Finite-element method (FEM) is a numerical technique for finding the approximate solutions to boundary value problems. Analogous to the idea of connecting many tiny straight lines to form a circle, FEM combines many simple element equations over many small subdomains, named finite elements, to approximate a more complex equation over a larger domain. For solar cell modeling, 2D simulations were performed using the APSYS simulator, which solves several interwoven

equations, including the Poisson's equation and the drift-diffusion equation for electron and holes using FEM. These finite elements are represented through mesh design in the device structures, wherein the density of mesh points and the spacing arrangement between various mesh points can be defined. For instance, the regions in a device which are more sensitive to the device performance can be assigned with more dense mesh design with mesh points closely spaced. In a solar cell, these high density mesh regions include most of the interfaces, the base layer and the tunnel junctions.

The optical propagations in a solar cell, related to the electron-hole generation due to the incident light, are modeled with the transfer matrix method and/or ray tracing by taking into account the reflections at the interfaces. The tunnel junction models incorporate complex Zener-type tunneling models. All important generation and recombination mechanisms, such as Shockley-Reed-Hall recombination (SRH), spontaneous and Auger recombination, were taken into account.

The most important equations solved by the simulator using FEM are the Poisson's equation and the continuity equation for electrons and holes. The Poisson's equation is as follows:

$$-\nabla.\left(\frac{\varepsilon_0\,\varepsilon_{dc}}{q}\ \nabla V\right) = -n + p + N_D(1 - f_D) - N_A\,f_A\ + \sum_j N_{tj}\ (\delta_j - f_{tj}\ ) \qquad (3.1)$$

where V is the electric potential, ε_o vacuum dielectric constant, ε_{dc} relative DC or low frequency dielectric constant, q electronic charge, n electron concentration, p hole concentration, N_D the shallow donor density, N_A the shallow acceptor density, f_D occupancy of the donor level, f_A occupancy of the acceptor level, N_{tj} the density of the jth deep trap, f_{tj} the occupancy of the jth

deep trap level, δ_j is 1 for donor-like traps and 0 for acceptor-like traps. The current continuity equation for electrons and holes are respectively expressed as:

$$\nabla . J_n - \sum_j R_n^{tj} - R_{sp} - R_{st} + R_{au} + G_{opt}(t) = \frac{\partial n}{\partial t} + N_D \frac{\partial f_D}{\partial t} \quad (3.2)$$

$$\nabla . J_p + \sum_j R_p^{tj} + R_{sp} + R_{st} + R_{au} - G_{opt}(t) = -\frac{\partial p}{\partial t} + N_A \frac{\partial f_A}{\partial t} \quad (3.3)$$

where J_n and J_p are electron and hole current flux density respectively. R^{tj}_n and R^{tj}_p are the electron and hole recombination rates per unit volume through the jth deep trap, respectively. G_{opt} is the optic generation rate, R_{sp}, R_{st}, and R_{au} are the spontaneous recombination rate, the stimulated recombination rate and the Auger recombination rate per unit volume, respectively.

3.2 Simulation Platform

The most important files in a simulation project include: (i) *layer file*, (ii) *sol file* and the (iii)

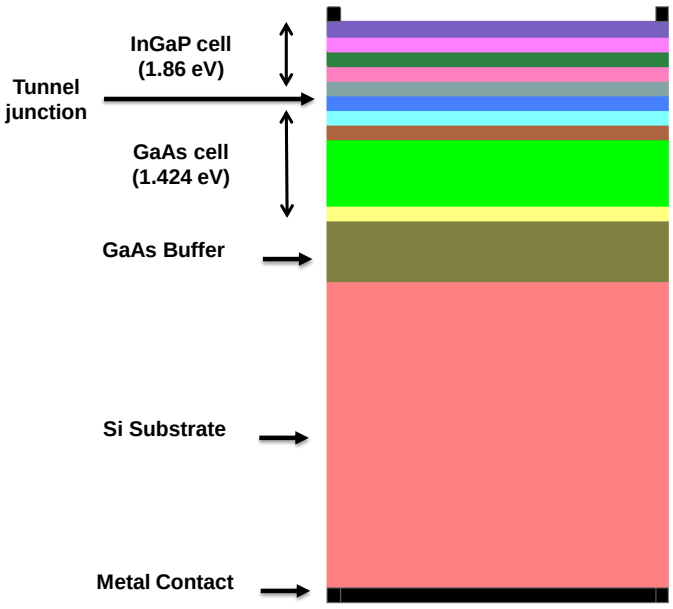

Figure 3.1 *LayerBuilder* schematic of 2J InGaP/GaAs solar cell on Si substrate.

plt file. The device structure is defined in the *layer file*, which can also be set up in the *LayerBuilder*. The *LayerBuilder* schematic of our 2J InGaP/GaAs solar cell structure on Si is shown in Figure 3.1. Multiple columns can be constructed which are useful in defining the metal contacts. The mesh design is defined in the *layer file*. Using the *layer file*, user can define the material composition, doping-type, doping concentration, layer thicknesses and metal contact (schottky vs. ohmic).

The *sol file* or the main solver lets the user define material parameters such as the band-gaps, minority carrier lifetimes, surface recombination velocities, tunnel junction position, anti-reflecting coating design as well as the associated reflection/transmission properties and the

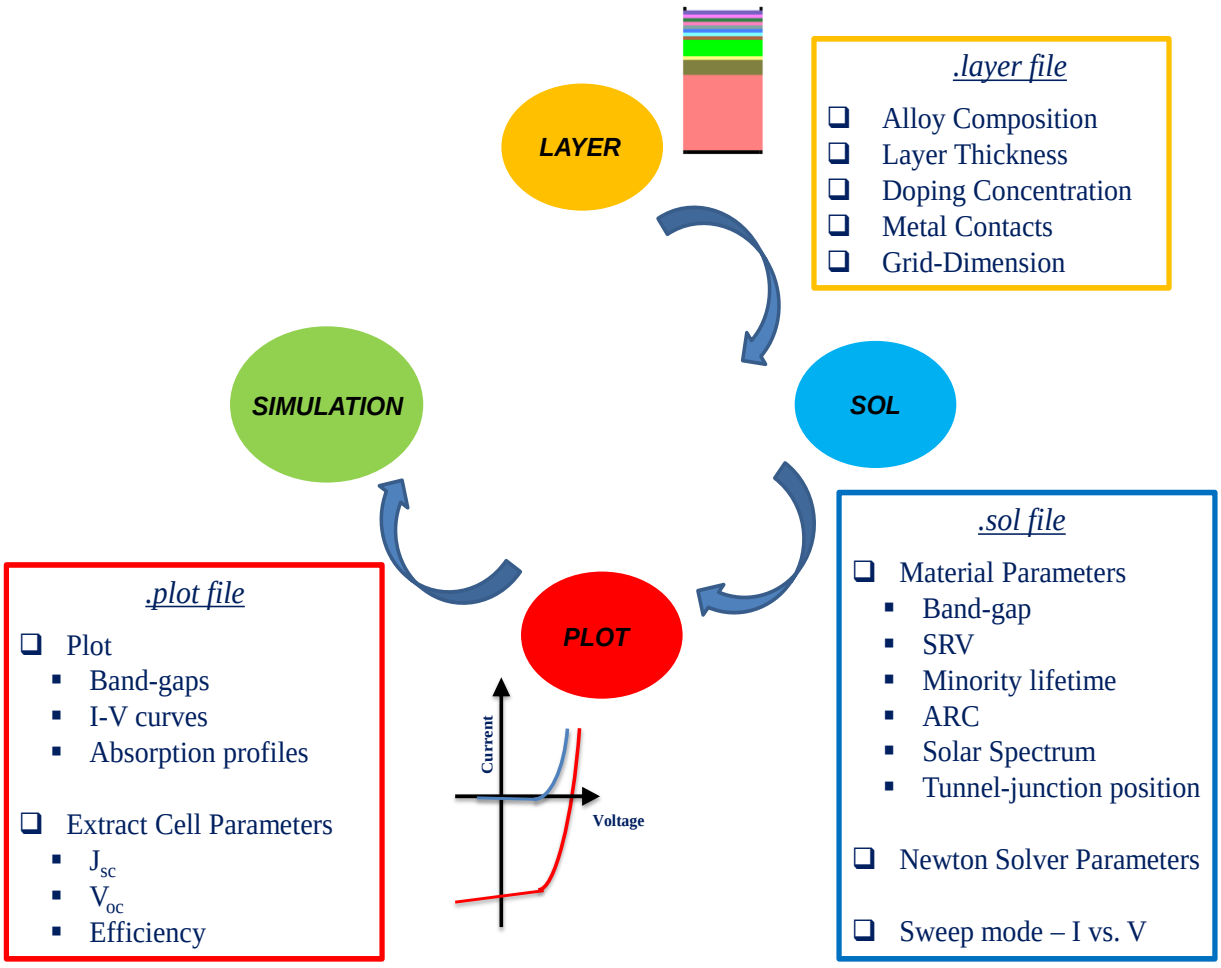

Figure 3.2 Flow chart of the modeling sequence in APSYS.

incident solar spectrum. The simulation parameters in terms of the current/voltage sweep range and step size are also defined in the *sol file*. The simulator generates files for the mesh, material and doping from the *layer file*. The main solver for simulating the device utilizes all of these files. The *plt file* lets the user define the plot description, the axis range and also allows the extraction of important solar cell parameters such as the η, V_{oc} and J_{sc}. The complete modeling sequence is described through a flow chart, as shown in Figure 3.2.

3.3 Dislocation-dependent Minority Carrier Lifetime Model

Minority carrier lifetime is one of the most important figure-of-merits for the design of metamorphic solar cells. Defects and dislocations are generated due to the lattice-mismatch between GaAs and Si substrate. These dislocations may serve as recombination centers and decrease the minority carrier lifetimes and hence the diffusion lengths. Typically, as the threading dislocation density increases, the minority carrier lifetime decreases. The effective minority carrier lifetime (τ_n or τ_p) in a lattice-mismatched system varies as a function of TDD (f (τ_{TDD})) [3], [4] and can be expressed as:

$$\frac{1}{\tau_{n,p}} = \frac{1}{\tau^{\circ}_{n,p}} + \frac{1}{\tau_{TDD}} \tag{3.4}$$

where τ°_p and τ°_n are the minority carrier lifetime for a dislocation free material. The τ_{TDD} is the minority carrier lifetime associated with the recombination at dislocation and can be expressed as:

$$\tau_{TDD} = \frac{4}{\pi^3 (TDD) D} \tag{3.5}$$

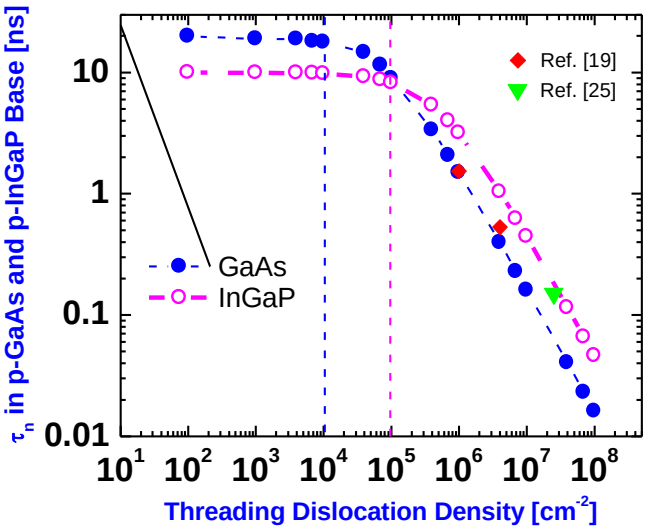

Figure 3.3 Correlation of threading dislocation density on the minority electron lifetime in p-GaAs and p-InGaP base.

where D is the minority carrier diffusion coefficient and TDD is the threading dislocation density in cm^{-2}.

The important solar cell parameters for modeling the performance of 2J InGaP/GaAs solar cells on Si are outlined in Table 3.1. The minority carrier mobility takes into account the effect

Parameters (Abbreviation, Units)	GaAs	InGaP
Band-gap (E_g, eV)	1.424	1.86
Minority electron mobility (μ_e', cm^2 Vs)	3088.8	1074 [9]
Minority hole mobility (μ_h', cm^2/Vs)	100 [7]	40 [9]
Electron diffusion coefficient (D_n, cm^2/s)	80 [8]	27.816
Hole diffusion coefficient (D_p, cm^2/s)	2.59	1.036
Peak minority electron lifetime (τ_n°, ns)	20 [3],[5]	10 [10],[12]
Minority hole lifetime (τ_p°, ns)	2.5	1
Surface Recombination Velocity (SRV, cm/s)	10^6	10^4

Table 3.1 Material and transport parameters for GaAs and InGaP solar cell materials.

of doping concentration. Using the dislocation-dependent minority carrier lifetime model described above, coupled with the material and transport parameters summarized in Table 3.1, we computed the impact of TDD on the minority electron lifetime in p-GaAs and p-InGaP base as shown in Figure. 3.3. Also, plotted in the graph are the experimental data points for minority electron lifetime in p-GaAs and p-InGaP, suggesting a close match between the model and the experiment [5], [6].

This degradation in minority carrier lifetime, from the dislocation-dependent minority carrier lifetime model, was utilized to incorporate the impact of TDD on the performance of III-V solar cells on Si (discussed in Chapter 4). From Figure 3.3, it can be noted that for TDDs greater than 10^4 cm^{-2} in GaAs subcell, the minority electron lifetime significantly degraded. The onset of degradation in minority electron lifetime occurs at a higher TDD (10^5 cm^{-2}) in InGaP subcell compared to GaAs subcell due to the lower electron diffusion coefficient in p-InGaP material. This suggests that GaAs subcell in a 2J InGaP/GaAs cell configuration is more sensitive to the dislocations than the InGaP subcell.

3.4 Modeling Assumptions

In a solar cell, most of the light is absorbed in the thick base and the minority carriers generated far away from the junction should have sufficient lifetime to reach the junction before they are recombined in the quasi-neutral region. Therefore, the variation of the minority electron lifetime in the base (τ_n) was found to have a significant impact on the cell performance. The minority hole lifetime (τ_p) in the thin emitter was considered to be constant. The impact of threading dislocations is much more severe on the minority carrier lifetime than the minority carrier mobility. In our model, the mobility of minority carriers was assumed to be independent

of TDD [4]. In reality the dislocations might impact the minority carrier mobility, however the measurement of minority carrier mobility is difficult and little data is available. Thus, the degradation in solar cell performance with increasing dislocation was assumed to be predominantly impacted by the degradation in the minority carrier lifetime. The minority carrier mobility and diffusion coefficients utilized for this modeling work are summarized in Table 3.1 along with the respective references. The surface recombination velocity (SRV) was set to 10^4 cm/s for both holes (S_p) and electrons (S_n) at InGaP base/back reflector interface and emitter/window interface. The corresponding S_n and S_p values were set to 10^6 cm/s at both the interfaces in the GaAs subcell.

The tunnel junctions, which are used as low-resistance connections between the subcells, may limit the overall cell performance if the current density in the solar cell (typically 14-15 mA/cm^2 at 1-sun) exceeds the peak tunneling current density of the tunnel diode. The tunnel junctions are typically very thin and heavily doped which makes it extremely challenging to estimate the minority carrier lifetimes needed to accurately model the impact of threading dislocations on their performance. Therefore, for the simplification of the analysis, the AlGaAs/GaAs tunnel junction employed in our cell structure was assumed to be unaffected at a TDD of $1x10^6$ cm^{-2}. This potential risk of reduction in peak tunneling current density of the tunnel diode as a result of threading dislocations could be mitigated by utilizing AlGaAs/GaAs based tunnel junctions with AlGaAs barrier layers, which have peak current density over 300 A/cm^2, equivalent to operation under a concentration of 20,000 suns [12]. Thus, based on some of these simplistic assumptions, the analysis discussed in this work provides an upper bound for the performance of metamorphic 2J InGaP/GaAs cell design on Si. The results are instructive for future design and optimization of multijunction metamorphic solar cell design on Si.

3.5 Model Calibration

In order to calibrate the dislocation-dependent minority carrier lifetime model and to validate our material parameters, we utilized experimental results from the state-of-the-art 2J InGaP/GaAs solar cell structures [13], [14]. The two most important parameters to accurately model the solar cell performance were the doping concentration and the layer thicknesses. Some of the parameters such as the band-gaps, surface recombination velocities, lifetimes and anti-reflecting coating design were best estimated when not available.

A minority electron lifetime of 5.2 ns in p-InGaP was reported in [13]. This value of lifetime corresponds to a TDD of $4x10^5$ cm^{-2} as shown in Figure 3.3. Since, the value of minority electron lifetime in p-GaAs was not provided; a τ_n value of 3.3 ns was used, as calculated in the Figure 3.3. Our simulation results are compared to the experimental results in the Table 3.2. Overall, the simulated and the experimental values presented in Table 3.2 are in excellent agreement, thus validating our model and the parameters utilized in the simulation.

	V_{oc} (V)	J_{sc} (mA/cm^2)	FF (%)	Efficiency (%)
Experiment [13]	2.48	14.22	85.6	30.28
Simulation	2.41	13.85	88.9	29.80
Experiment [14]	2.52	12.70	85.00	27.20
Simulation	2.58	12.53	85.19	27.64

Table 3.2 Model Calibration with experimental data for 2J InGaP/GaAs solar cells.

CHAPTER 4

DESIGN OF III-V SOLAR CELLS ON Si SUBSTRATE

N. Jain and M.K. Hudait, (2013) "Impact of Threading Dislocations on the Design of GaAs and InGaP/GaAs Solar Cells on Si Using Finite Element Analysis, " *IEEE Journal of Photovoltaics,* vol. 3, 2013, pp. 528. First author retained copyright.

N. Jain and M.K. Hudait, "Design of metamorphic dual-junction InGaP/GaAs solar cell on Si with efficiency greater than 29% using finite element analysis," in *Proc.* 38th IEEE Photovoltaic Spec. Conf., 2012, pp. 002056. First author retained copyright.

The modeling of 1J n+/p GaAs and 2J n+/p InGaP/GaAs solar cell on Si substrate was performed under the AM1.5G spectrum (1000 W/m^2) and a bilayer MgF_2/ZnS anti-reflective coating was used. A low-resistance AlGaAs/GaAs tunnel junction was employed to connect the individual GaAs and InGaP subcells in the 2J configuration. Other important material and transport materials were used as described in the Table 3.1 in the Chapter 3. The thickness of the initial nucleation layer and the GaAs buffer layer was considered as 2.5 μm (greater than the critical layer thickness for GaAs on Si). The separation between the front metal gridlines was set as 500 μm. The entire structure above the GaAs buffer layer was designed to be internally lattice-matched to the GaAs buffer. However, all the threading dislocations, which were generated due

to the 4% lattice-mismatch between GaAs and Si, were considered to propagate into the top InGaP subcell as well.

In order to compute the impact of threading dislocations on the performance of 1J n+/p GaAs and 2J n+/p InGaP/GaAs solar cell on Si substrate, we utilized our calibrated dislocation-assisted model, which was described in Chapter 3. The degradation in minority electron lifetime in the base, as a function of increasing threading dislocation, was incorporated to investigate the cell performance. In the sections 4.1 and 4.2, the impact of minority carrier lifetime degradation on the performance of 1J GaAs cell on Si and 2J InGaP/GaAs cell on Si are discussed. Emphasis was made on the cell performance at a realistic TDD of 10^6 cm^{-2} for GaAs on Si [1]. Section 4.3 presents our approach of engineering the 2J InGaP/GaAs solar cell design on Si to realize current-matching between each subcell at a TDD of 10^6 cm^{-2}. Finally, section 4.4 will discuss the impact of surface recombination on the 2J cell performance.

4.1 Single-Junction GaAs Solar Cell on Si Substrate

The schematic of 1J n+/p GaAs solar cell on Si substrate is shown in the Figure 4.1(a). The p-GaAs base thickness in the 1J n^+/p GaAs cell on Si was initially set to 2.5 μm. This thickness of 2.5 μm for GaAs base has been previously used in the high efficiency inverted metamorphic triple-junction (3J) solar cells based on lattice-matched InGaP and GaAs subcells and lattice-mismatched InGaAs subcell on GaAs substrate [2]. In our analysis, the TDD in this GaAs cell was varied from 10^4 cm^{-2} to 10^8 cm^{-2}. At a TDD of 10^6 cm^{-2}, the minority electron lifetime in p-GaAs was calculated to be 1.49 ns, as shown in Figure 3.3, consistent with the experimentally determined minority electron lifetime of 1.5 ns in p-GaAs [3]. The band-diagram of the 1J GaAs solar cell under equilibrium was plotted earlier in chapter 2 (Figure 2.5). The corresponding

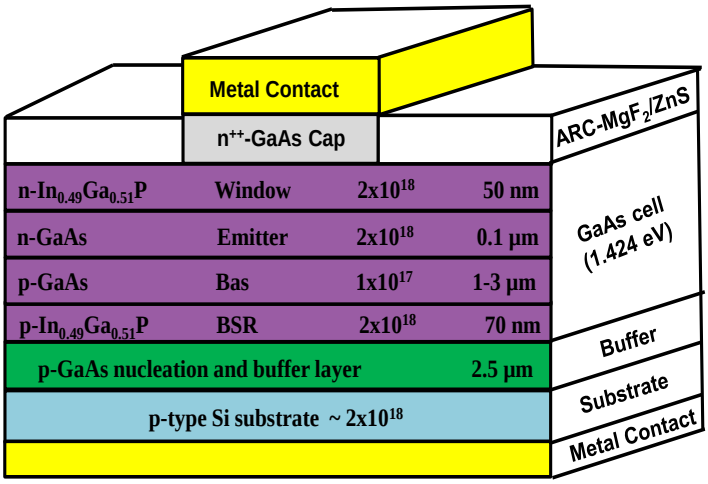

Figure 4.1 (a) Schematic depiction of 1J GaAs solar cell on Si with the base thicknesses in the GaAs subcell as 2.5 µm.

band-diagram of the 1J GaAs solar cell under illumination (or forward bias) is plotted in Figure 4.1 (b), clearly indicating the split in the Fermi level into the two quasi-Fermi levels on the n-side and the p-side.

Voltage at maximum power point, V_m and V_{oc} were plotted as a function of increasing TDD in the 1J GaAs cell on Si as shown in the Figure 4.2 (a). At lower TDD, the higher values of both

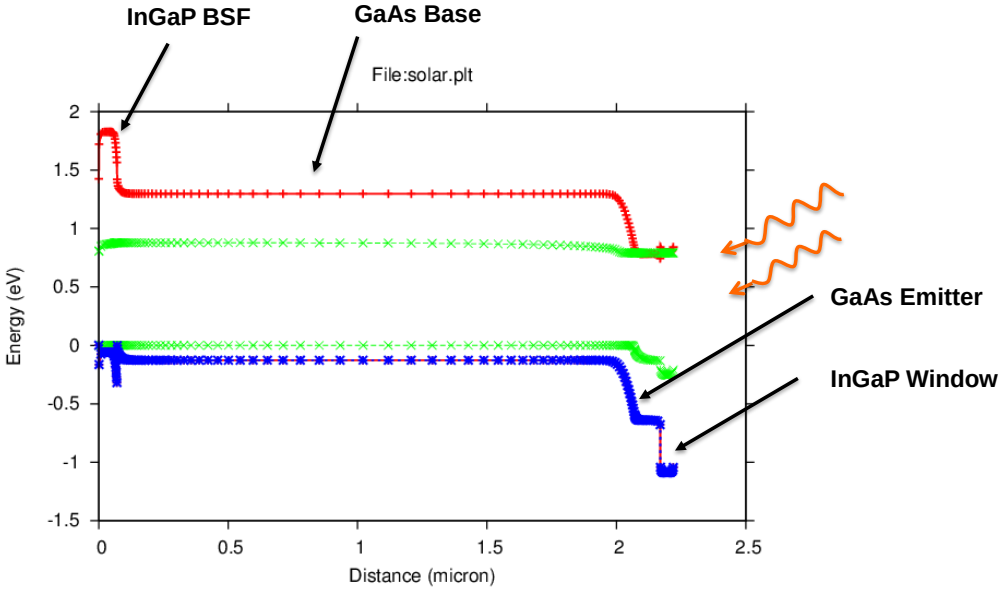

Figure 4.1 (b) Band gap of 1J n+/p GaAs solar cell under illumination.

V_{oc} and V_m were attributed to the higher minority electron lifetime in the p-GaAs base. Epitaxial structures with TDD below 10^4 cm^{-2} can be almost considered as lattice-matched. A TDD below 10^5 cm^{-2} had a negligible impact on the V_{oc}. However, beyond this TDD, V_{oc} started to degrade significantly. V_{oc} has a logarithmic dependence on reverse saturation current density, J_0 which is inversely proportional to the minority carrier lifetime. Thus, at higher TDD, significant degradation in both V_{oc} and V_m was attributed to the higher reverse saturation current density pertaining to the reduced minority electron lifetime.

Current density at maximum power point, J_m and J_{sc} were plotted as a function of TDD in the 1J GaAs cell on Si as shown in Figure 4.2 (b). For a TDD below $4x10^5$ cm^{-2}, the minority

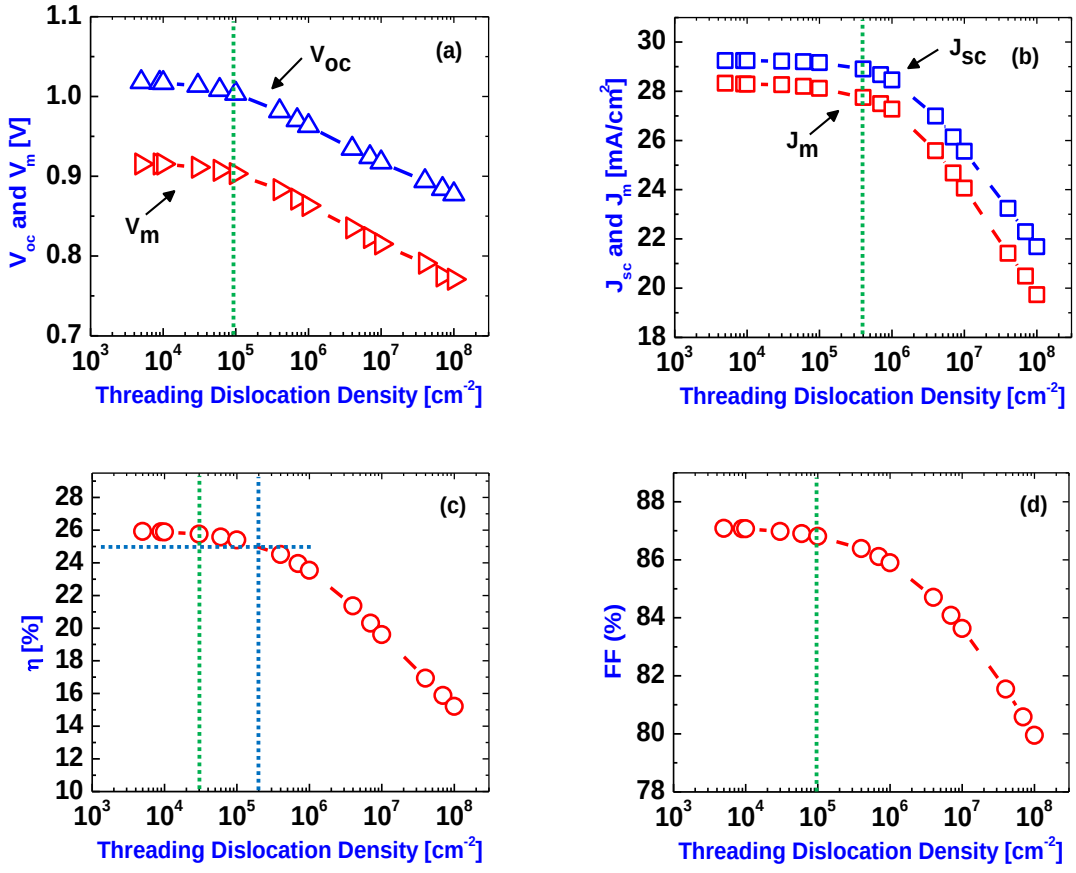

Figure 4.2 Impact of threading dislocation density variation on the performance of 1J GaAs solar cell on Si: (a) V_{oc} and V_m, (b) J_{sc} and J_m, (c) η and (d) FF under AM1.5G spectrum.

electrons had sufficient lifetime to reach the junction before being recombined and hence, TDD below $4x10^5$ cm^{-2} had a negligible impact on the J_{sc}. For the 1J GaAs cell considered here, a minority electron lifetime of at least 0.78 ns (at a TDD of $2x10^6$ cm^{-2}) was necessary for the cell to function as a short diode. Beyond a TDD of $2x10^6$ cm^{-2}, the cell behaved like a long diode with the electron diffusion length becoming shorter than the GaAs base thickness. Thus, beyond a TDD of $2x10^6$ cm^{-2}, the degradation in both J_{sc} and J_m was attributed to the reduction in minority electron lifetime. Interestingly, from Figure 4.2 (a) and (b), it can be seen that the beginning of degradation in J_{sc} occurred at a higher TDD than V_{oc}, indicating J_{sc} was more tolerant to TDD in the 1J GaAs solar cell on Si.

The fill factor as a function of increase in TDD was plotted in Figure 4.2 (d). There was almost negligible drop in fill factor for TDD lower than 10^5 cm^{-2}. The percentage drop in both J_m and V_m from a TDD of 10^4 cm^{-2} to 10^8 cm^{-2} was greater than the percentage drop in J_{sc} and $V_{oc,}$ respectively, as can be see from Figure 4.2 (a) and (b). Thus, at higher TDD, a greater percentage drop in the J_m*V_m product compared to $J_{sc}*V_{oc}$, led to the degradation in FF. This degradation in FF in turn limited the performance of the 1J GaAs solar cell on Si at higher dislocation densities.

Figure 4.2 (c) shows the degradation in efficiency of the 1J GaAs solar cell on Si as a function of increasing TDD. It can be seen that cell efficiency higher than 25% were attained for TDD below $2x10^5$ cm^{-2} (or τ_n greater than 5 ns). The highest efficiency for our 1J GaAs cell was ~26%, while the record efficiency for GaAs solar cell is 28.8% [4]. One of the main reasons for this difference in performance could be attributed to the thin-film cell design for the record efficient cells, which were epitaxially released from the host substrate. Anti-reflective coating design and photon recycling design could have also attributed to the difference in the efficiency.

Beyond a TDD of ~10^5 cm^{-2}, the cell efficiency significantly degraded due to the reduction in both J_m and V_m, as discussed earlier. At an experimentally realistic TDD of 10^6 cm^{-2} [1], the corresponding cell efficiency was found to be 23.54%, about an absolute 3% lower efficiency when the cell had minimal dislocations (less than 10^4 cm^{-2} can be considered almost lattice matched). At a higher TDD of 10^7 cm^{-2}, the corresponding cell efficiency degraded to 19.61% due to the drastic reduction in the minority electron lifetime. This efficiency was about an absolute 6% lower than the performance of the lattice-matched GaAs solar cell, thus, suggesting that 1J GaAs solar cell are extremely sensitive to threading dislocations. Thus, it was important to investigate the performance of multijunction (dual-junction or more) solar cells on Si substrate to exploit the advantage of integration with Si substrate.

4.2 Dual-Junction InGaP/GaAs Solar Cells on Si Substrate

For the analysis of metamorphic 2J n^+/p InGaP/GaAs solar cell on Si, the base thicknesses in the GaAs and InGaP subcells were set to 2.5 μm and 0.9 μm, respectively [2]. The schematic of

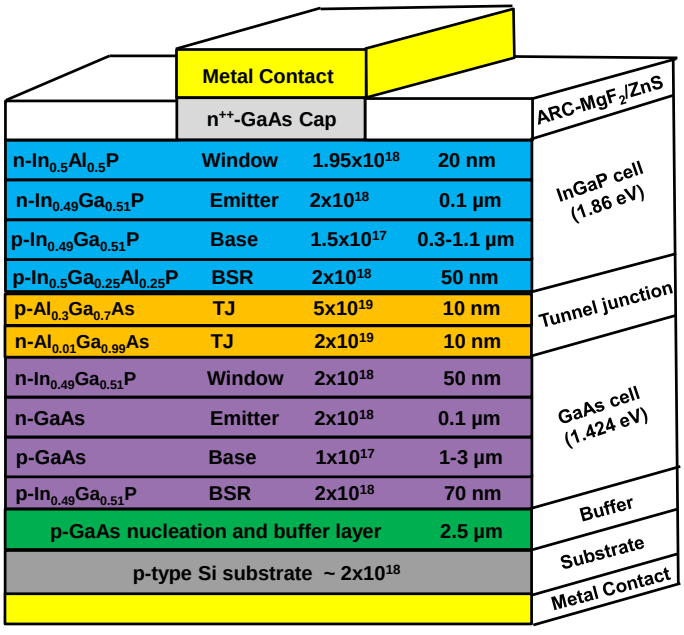

Figure 4.3 (a) Schematic depiction of 2J InGaP/GaAs solar cell on Si with the base thicknesses in the GaAs and InGaP subcells as 2.5 μm and 0.9 μm, respectively.

the 2J InGaP/GaAs solar cell structure on Si is shown in Figure 4.3 (a) and the corresponding band-diagrams at equilibrium and under illumination are shown in the Figure 4.3 (b) and (c), respectively. The TDD was varied from 10^5 to 10^8 cm^{-2} and it was assumed that all the threading dislocations in GaAs bottom subscell propagated to the top InGaP subcell, in spite of the top InGaP subcell grown lattice-matched to the bottom GaAs subcell.

Figure 4.4 (a) shows the degradation in both V_{oc} and V_m as a function of increasing TDD in the 2J InGaP/GaAs solar cell on Si. The primary reason for the decrease in V_{oc} was attributed to

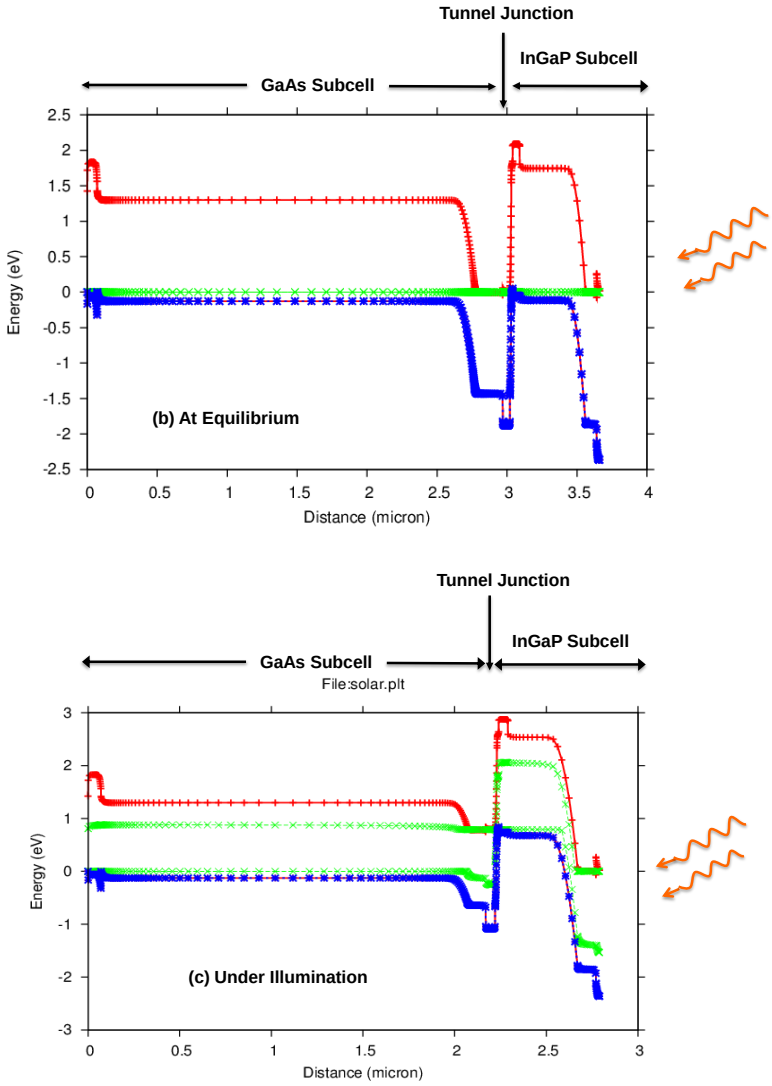

Figure 4.3 Band gap of 2J n+/p InGaP/GaAs solar cell (b) under equilibrium and (c) under illumination.

the strong dependence on the reverse saturation current density, J_{02}, associated with the depletion region recombination. The V_{oc} can be expressed as,

$$V_{oc} = \frac{n_2 kT}{q} ln\left(\frac{J_{sc}}{J_{02}}\right) \tag{4.1}$$

where, J_{02} depends on the minority carrier base lifetime, τ_{base} and is expressed as,

$$J_{02} = \frac{qn_i W_D}{2}\left(\frac{1}{\tau_{base}}\right) \tag{4.2}$$

where, n_i is the intrinsic carrier concentration and W_D is the depletion layer width. At higher

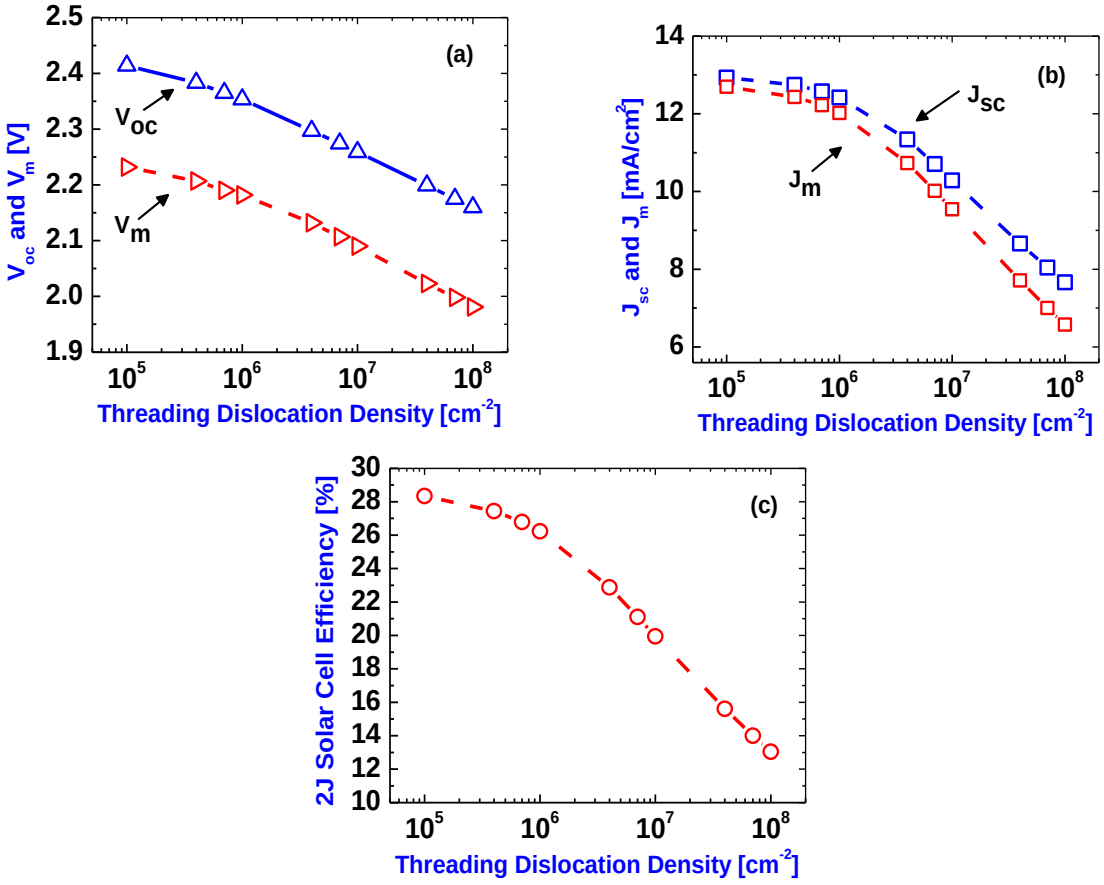

Figure 4.4 Impact of threading dislocation density variation on the performance of 2J InGaP/GaAs solar cell on Si: (a) V_{oc} and V_m, (b) J_{sc} and J_m and (c) η under AM1.5G spectrum.

TDD, the value of J_{02} increased due to the reduction in minority electron lifetime. Thus, the increase in J_0 led to significant degradation in both V_{oc} and V_m with increasing TDD.

The corresponding J_{sc} and J_m in the 2J InGaP/GaAs solar cell on Si were plotted as a function of increase in TDD in Figure 4.4 (b). The degradation in both J_{sc} and J_m at higher TDD was due to the simultaneous reduction in the minority electron lifetime in both GaAs and InGaP base. The onset of degradation in J_{sc} in 2J cell configuration was also found to occur at higher TDD compared to V_{oc}, similar to the 1J GaAs cell, which was discussed in section 4.1. Thus, J_{sc} was found to be more tolerant to TDD compared to V_{oc} for both 1J GaAs and 2J InGaP/GaAs cells on Si. This clearly indicates that the performance of metamorphic solar cells was more impacted by the degradation in V_{oc} compared to the degradation in J_{sc}.

Figure 4.4 (c) shows the degradation of 2J InGaP/GaAs cell efficiency as a function ofincreasing TDD. The efficiency of our lattice-matched 2J InGaP/GaAs solar cell was about 28.5% compared to the record efficient 2J InGaP/GaAs cells with an efficiency of about 30.8%. At a realistic TDD of 10^6 cm^{-2} in our 2J structure on Si, the corresponding 2J cell efficiency was 26.22%. Beyond a TDD of 10^6 cm^{-2}, the degradation in minority electron lifetime in the p-GaAs significantly hindered the 2J InGaP/GaAs cell efficiency as the GaAs subcell was more sensitive to dislocations compared to InGaP (see Figure 3.3). Beyond a TDD of 10^7 cm^{-2}, the 2J InGaP/GaAs solar cell efficiency degraded to that of 1J GaAs cell efficiency, thus, making the contribution of the top InGaP cell redundant. Hence, it is extremely important to achieve TDD lower than 10^7 cm^{-2} to be able to take the advantage of dual-junction cell design on Si.

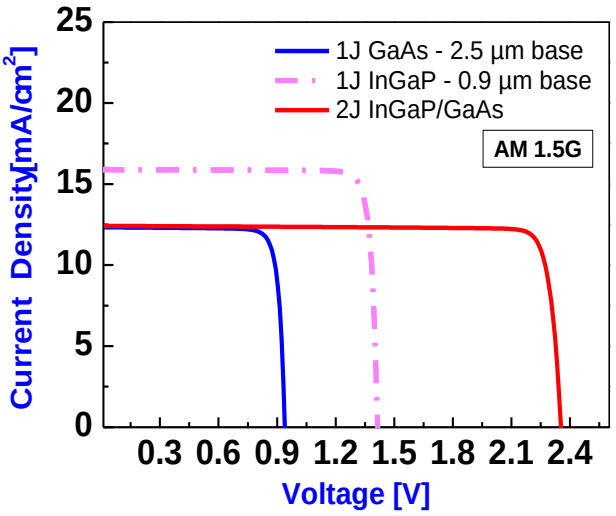

Figure 4.5 J-V characteristic of 2J cell along with the InGaP and GaAs subcell before current-matching at a TDD of 10^6 cm^{-2} at AM 1.5G.

The J-V characteristics of 2J InGaP/GaAs (red curve) cell, the GaAs subcell (blue curve) and the InGaP subcell (pink curve) are plotted in the Figure 4.5 at a TDD of 10^6 cm^{-2}. It can be seen that when the GaAs and InGaP base thicknesses were set to 2.5 µm and 0.9 µm, respectively, the subcells were not current-matched and the bottom GaAs subcell limited the J_{sc} in the 2J cell configuration. In practice, it is challenging to improve the material quality of heteroepitaxial GaAs grown on Si to lower the TDD significantly below 10^6 cm^{-2}. Consequently, it becomes extremely important to optimize the metamorphic 2J InGaP/GaAs cell structure on Si at a realistic TDD of 10^6 cm^{-2} by tailoring the design of each subcell to realize the current-matching between them.

4.3 Current-Matching in Dual-Junction InGaP/GaAs Solar Cells on Si

In a multijunction cell, one of the most important design criteria is to achieve the current-matching between the subcells. Current-matching enables to extract the best performance from a multijunction cell. The cell with a higher band-gap provides a higher V_{oc} and lower J_{sc}. For

achieving the current-matching condition, ideally J_m between each subcell should be matched. Here, we used J_{sc} for current-matching as J_{sc} is a directly measurable parameter during cell characterization and it has been widely used for current-matching analysis [5], [6].

The subcells in our initial 2J solar cell design were not current-matched as shown in Figure 4.5. Therefore, appropriate design changes in our 2J cell structure were required to realize the current-matching condition between the subcells. In a solar cell, most of the light in absorbed in the thicker base layer and, hence, the minority carrier lifetime in the base plays a critical role in determining the current density contribution from each subcell. Thus, we optimized the base thicknesses in the GaAs and the InGaP subcells to achieve the current-matching condition at an experimentally realistic TDD of 10^6 cm^{-2} [1]. At this TDD, the value of τ_n calculated was as 1.494 ns and 3.171 ns in the p-GaAs and the p-InGaP base, respectively, as shown in Figure 3.3.

We first varied the thickness of p-InGaP base from 0.3 μm to 1.1 μm in 1J InGaP solar cell configuration. This is represented by the blue curve in the Figure 4.6 (a). Then, in the 2J cell configuration, the thickness of p-InGaP base was again varied over the same range with the

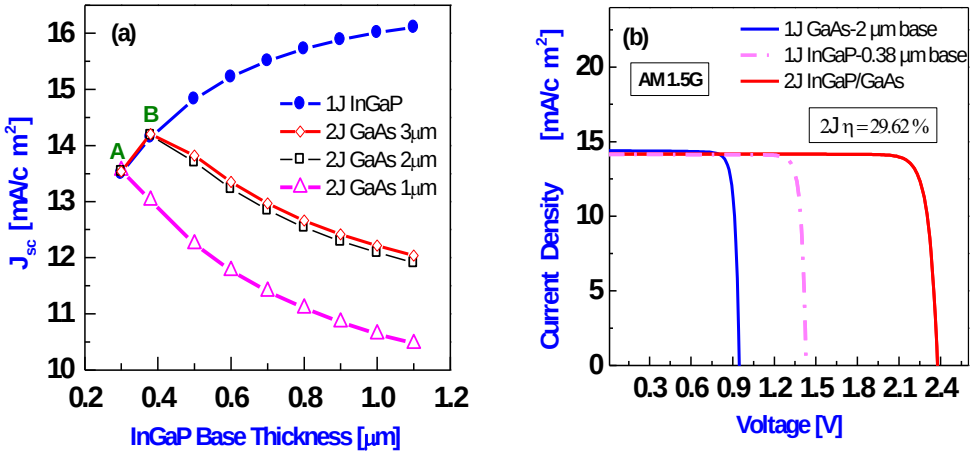

Figure 4.6 (a) Short-circuit current density as a function of top InGaP base thickness to optimize top and bottom cell base thicknesses for current- matching, (b) Current-matched J-V characteristic in a 2J InGaP/GaAs solar cell at AM 1.5G corresponding to the current-matched point B in Figure 4.6 (a).

GaAs base thickness set to 1 μm (pink curve) as shown in Figure 4.6 (a). The same procedure was repeated for the GaAs base thickness of 2 μm (black curve) and 3 μm (red curve). The InGaP solar cell structure was the same in both the 1J InGaP and the 2J InGaP/GaAs cell configurations. It can be seen that thinning the base thickness in 1J InGaP solar cell lowered the J_{sc} due to reduction in the absorption depth for the photons to be absorbed in the p-InGaP base. Interestingly, thinning the InGaP base thickness in the 2J cell configuration allowed more photons through to the bottom GaAs subcell, resulting in an increase of J_{sc} in the GaAs subcell at the cost of reduction in J_{sc} from the InGaP subcell. This resulted in the overall increase in J_{sc} of 2J cell as the bottom GaAs subcell limited the J_{sc} in the 2J cell configuration. Furthermore, as the top cell base was being thinned, increase in the base thickness of the bottom GaAs subcell allowed additional photons through to the GaAs subcell. This led to further improvement in the overall J_{sc} of the 2J cell. However, further increment in the GaAs base thickness beyond 2 μm did not result in significant improvement of J_{sc}. This was likely due to insignificant photocurrent contribution from the GaAs subcell beyond a base thickness of 2 μm. The saturation of light absorption in GaAs beyond a thickness of 2 μm was ruled out as it can be clearly seen from the Figure 4.7 that the optical generation rate in the GaAs cell was not negligible beyond a base thickness of 2 μm. Hence, the minimal increase in J_{sc} by increasing the GaAs base thickness beyond 2 μm was related to inefficient carrier collection.

Utilizing the method discussed above, the current-matching condition was realized at point A (J_{sc}=13.5 mA/cm^2) and B (J_{sc}=14.18 mA/cm^2), as shown in Figure 4.6 (a). The J-V characteristics of the 2J cell and the individual subcells corresponding to the point B were plotted in Figure 4.6 (b). At point B, the 2J cell exhibited a conversion efficiency of 29.62% with a 2 μm and a 0.38 μm thick GaAs and InGaP base, respectively. The cell parameters extracted after

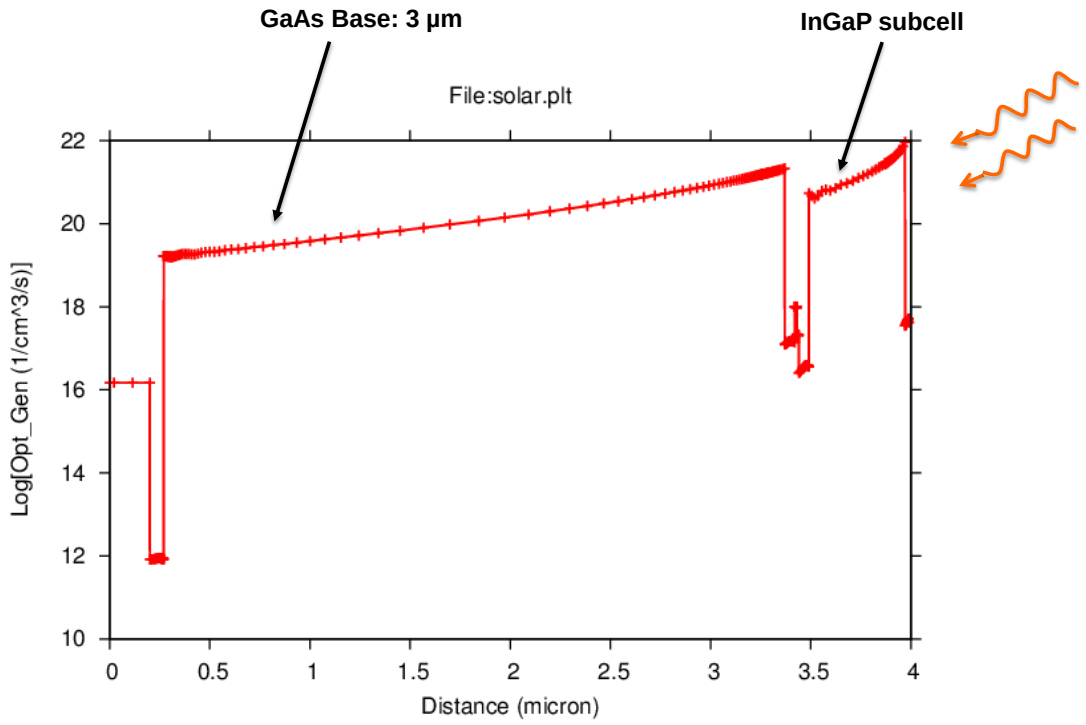

Figure 4.7 Optical generation rate in the 2J InGaP/GaAs solar cell as a function of cell depth.

achieving the current-matching condition between the two subcells at a TDD of 10^6 cm^{-2} were summarized in Table 4.1. These results illustrate that even at a TDD of 10^6 cm^{-2}, an efficiency of greater than 29% can be realized for a metamorphic 2J InGaP/GaAs solar cell on Si by carefully engineering the cell design.

2J InGaP/GaAs solar cell (InGaP/GaAs base thickness in µm)	**V_{oc} (V)**	**J_{sc} (mA/cm²)**	**FF (%)**	**Efficiency (%)**
Before optimization (0.9/2.5)	2.35	12.41	89.73	26.22
After optimization (0.38/2.0)	2.37	14.18	88.22	29.62

Table 4.1 Parameters for 2J InGaP/GaAs solar cell on Si: before and after optimization under AM1.5G.

4.4 Impact of Surface Recombination on the Cell Performance

Interface recombination could be a major factor limiting the performance of a tandem cell. Recombination at top InGaP subcell interfaces was found to have the most detrimental impact on the overall performance of a 3J InGaP/GaAs/Ge solar cell [7]. In our design, the thickness of the top InGaP subcell was significantly reduced; hence, it was important to analyze the impact of surface recombination velocity (SRV) on the overall 2J cell performance. Figure 4.8 shows the impact of SRV at top InGaP subcell interfaces on the 2J cell cell η and J_{sc}. Initially, all the SRVs were set to 10^0 cm/s at all the interfaces in the GaAs and the InGaP subcells. Thereafter, the SRV was set to 10^6 cm/s in the GaAs subcell, while the SRV in the InGaP subcell was varied. It can be seen that the SRV, when below 10^4 cm/s in the InGaP subcell, had negligible impact on the efficiency of the 2J solar cell. However, the efficiency dropped to 27.35% at a SRV of 10^6 cm/s due to degradation in J_{sc}. Thus, it can be concluded that an additional design consideration to be kept in mind for designing metamorphic 2J InGaP/GaAs solar cells on Si substrate is to restrict the SRV below 10^4 cm/s in the InGaP subcell to achieve high efficiency 2J InGaP/GaAs solar

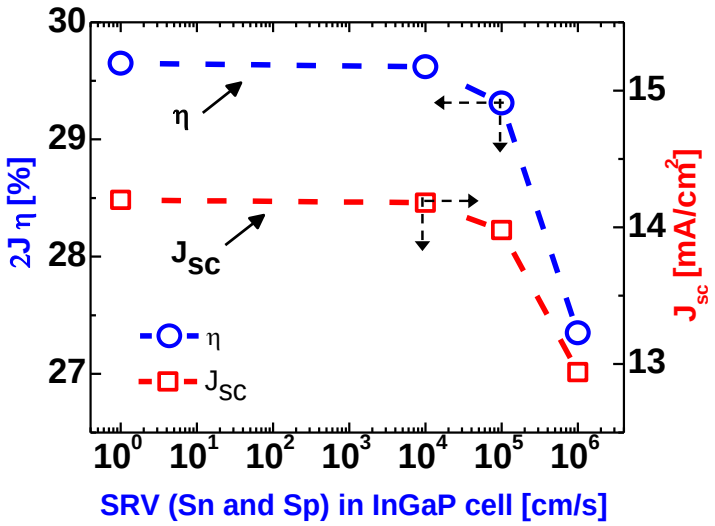

Figure 4.8 2J InGaP/GaAs cell η and J_{sc} as a function of SRV in the top InGaP subcell.

cells on Si substrate.

The results of the modeling work presented in this thesis were published and the copies are available online [8], [9].

CHAPTER 5

CONCLUSION AND FUTURE WORK

5.1 Conclusion

In this thesis, we have comprehensively investigated the impact of threading dislocations density on the performance of 1J n^+/p GaAs and 2J n^+/p InGaP/GaAs solar cell on Si substrate at AM 1.5G spectrum. 1J GaAs solar cell on Si with a 2.5 μm thick GaAs base exhibited an efficiency of ~23% at a realistic TDD of 10^6 cm^{-2}. For both 1J and 2J cell configurations, the onset of degradation in V_{oc} was found to occur at a lower TDD than in J_{sc}, indicating that V_{oc} was more sensitive to threading dislocation density as compared to J_{sc}.

The 2J InGaP/GaAs solar cell at a TDD of 10^6 cm^{-2} exhibited an efficiency of 26.22% with a 2.5 μm and 0.9 μm thick GaAs and InGaP base, respectively. The design of the 2J InGaP/GaAs cell on Si was optimized at a TDD of 10^6 cm^{-2} to achieve current-matching between the two subcells. By thinning the base thickness in the top InGaP subcell from 0.9 μm to 0.38 μm, the 2J cell efficiency increased to 29.62% from 26.22%. In the 2J configuration, we found that the GaAs subcell was more sensitive to dislocations and hence limited the overall short-circuit current density in the 2J configuration. At the interfaces in the top InGaP subcell, the surface recombination velocities below 10^4 cm/s were found to have negligible impact on the 2J cell

performance. The theoretical conversion efficiency of 29.62% for 2J InGaP/GaAs solar cell on Si substrate is comparable to the record efficiency of 30.8% for thin-film 2J InGaP/GaAs solar cells on GaAs substrate. Thus, even in a lattice-mismatched 2J InGaP/GaAs cell on Si with TDD of 10^6 cm^{-2}, a theoretical conversion efficiency of greater than 29% at AM1.5G was achieved by tailoring the device design.

While III-V tandem cells on Si are sensitive to dislocations, careful design and optimization of 2J InGaP/GaAs solar cells on Si can enable theoretical conversion efficiency of ~29% at TDD of 10^6 cm^{-2} under AM1.5G (1 sun), suggesting an optimistic future for direct integration of III-V solar cells on Si substrate. Once experimentally realized, this technology would offer a new paradigm for the advancement of low cost III-V solar cells and foster innovative avenues to harness the excellent energy conversion properties of III-V semiconductors with the volume manufacturability of Si.

5.2 Future Work

Although the modeling results presented in this thesis are encouraging for future design and optimization of metamorphic III-V solar cells on Si substrate; however, successful experimental demonstration of high quality GaAs growth on Si would be vital. The material characterization and analysis, especially the tunneling electron microscopy and the minority carrier lifetime measurements for III-V materials on Si will be important steps towards the realization of high quality III-V epitaxial films on Si. Once the epitaxial material stack is optimized, the fabrication and testing of 1J GaAs and 2J InGaP/GaAs solar cells on Si substrate will provide key insights into our modeling results. The experimental results will also provide necessary feedback for

further optimization of our model and the associated parameters to further improve the cell performance.

The ideal band gap combination for 3J III-V solar cell is ~1.86 Ev/1.42 eV/1.0 eV. Although, the band gap of Si is 1.1 eV, slightly higher the ideal band gap of 1 eV for the bottom subcell; however, it will be interesting to investigate silicon cell design for realizing a 3J InGaP/GaAs/Si solar cell structure on Si substrate. The Si bottom subcell could either be fabricated using standard diffusion processes or we could explore the possibility of utilizing the arsenic and/or gallium diffusion into the Si substrate during III-V material growth.

5.3 Scope

Direct integration of III-V compound semiconductors on large diameter, cheaper and readily available Si substrate is highly desriable for increased density, low-cost & lightweight photovoltaics. III-V integration on Si combines the excellent optical properties of compound semiconductors with the volume manufacturability of silicon allowing a path for significantly driving down the cell cost. III-V on Si technology is also attractive from the point of view of integration with commercially available substrate re-use techniques for additional cost savings such as the spalling [1] and the epitaxial lift-off techniques [2]-[4]. Furthermore, the direct GaAs on Si epitaxy would enable this approach to be easily extended and employed in conjunction with the current record efficient 3J solar cells utilizing dilute nitride bottom cell [5] as well as with the current state-of-the-art IMM triple junction solar cell [6] production lines. GaAs on Si solar cell technology could also be extended for concentrated photovoltaic (CPV) applications as utilization of GaAs based solar cells on Si substrate under higher concentration enables the cell to operate in a regime where the open-circuit voltage (V_{oc}) is dominated by the (n=1) diffusion

current and not by the (n=2) recombination current due to the dislocations [7], allowing more favorable utilization of III-V solar cells on Si for concentrated photovoltaic applications.

REFERENCES

CHAPTER 1

[1] J. Luther, World in transition – towards a sustainable energy system, German Advisory Council on Global Change (WBGU), pp.3.

[2] R. R. King, et al., "40% efficient metamorphic GaInP/GaInAs/Ge multijunction solar cells," *Appl. Phys. Lett*., vol. 90, 2007 pp. 183516-1.

[3] C. E. Fritts, "On a new form of selenium photocell," *Proceedings of the American Association for the Advancement of Science.*, vol. 33, 1883, p. 97.

[4] R. S. Ohl, "Light-sensitive electric device including silicon," *U. S. Patent 2,443,542*, June 27, 1941.

[5] H. J. Queisser, "Detailed balance limit for solar cell efficiency," *Materials Science and Engineering: B*, vol. 159–160, 2009, pp. 322.

[6] M. A. Green et al., "Solar cell efficiency tables (version 41)," *Progress in Photovoltaics: Research and Applications*, vol. 21, 2013, pp. 1.

[7] National Renewable Energy Laboratory Website - http://www.nrel.gov/ncpv/.

[8] N.V. Yastrebova et al., "High-efficiency multijunction solar cells: Current status and future potential," University of Ottawa, 2007.

[9] R. R King, et al., "Pathways to 40 percent-efficient concentrator photovoltaics, " *Proceedings of the 20th European Photovoltaic Solar Energy Conference*, Barcelona, Spain, 2005.

[10] M. Wanlass, et al., "Monolithic, ultra-thin GaInP/GaAs/GaInAs tandem solar cells," *4th World Conference on Photovoltaic Energy Conversion*, 2006, pp. 729..

[11] I. Garcia, et al., "A 32.6% efficient lattice-matched dual-junction solar cell working at 1000 suns," *Applied Physics Letters*, vol. 94, 2009, pp. 053509.

[12] J. F. Geisz, et al., "40.8% efficient inverted triple-junction solar cell with two independently metamorphic junctions," *Appl. Phys. Lett*., vol. 93, 2008, pp. 123505-1.

[13] V. Sabnis, et al., "High-efficiency multijunction solar cells employing dilute nitrides," *AIP Conference Proceedings*, vol. 1477, 2012, pp. 14.

[14] P. Wurfel, "Thermodynamic limitations to solar energy converstion," *Physica E: Low-Dimensional Systems and Nanostructures*, vol. 14, 2002, pp. 18.

[15] D. Shahrjerdi, et al., "High-efficiency thin-film InGaP/InGaAs/Ge tandem solar cells enabled by controlled spalling technology, " *Applied Physics Letters*, vol. 100, 2012, pp. 53901.

[16] B. Furman, et al., "A high concentration photovoltaic module utilizing micro-transfer printing and surface mount technology, " *in 35th IEEE Photovoltaic Specialists Conference*, 2010, p. 475.

[17] R. Tatavarti, et al., "InGaP/GaAs/InGaAs inverted metamorphic (IMM) solar cells on 4" epitaxial lifted off (ELO) wafers, " in *35th IEEE Photovoltaic Specialists Conference*, 2010, p. 2125.

[18] G. J. Bauhuis, *et al.*, "Wafer reuse for repeated growth of III–V solar cells," *Prog. Photovoltaics: Res. Appl.*, vol. 18, 2010, pp. 155.

[19] S. M. Vernon, et al., "High-efficiency concentrator cells from GaAs on Si," in *Proc. 22nd IEEE Photovoltaic Spec. Conf*, 1991, pp. 353.

[20] I. Mathews, et al., "Theoretical performance of multi-junction solar cells combining III-V and Si materials," *Opt. Express*, vol. 20, 2012, pp. A754.

[21] M. L. Lovejoy, et al., "Minority hole mobility in GaAs," in M.R. Brozel and G.E. Stillman (eds.), *Properties of Gallium Arsenide, Data Review Series no. 16*, London: INSPEC, 1996, pp. 123.

[22] M. S. Lundstrom, "Minority carrier transport in III-V semiconductors," in R.K. Willardson, A.C. Beer, and E.R. Weber (eds.), *Minority Carrier in III-V Semiconductors: Physics and Applications, Semiconductors and* Semimetals, vol. 39: Academic Press Inc., 1993, pp.193.

[23] C. L. Andre, et al., "Impact of dislocations on minority carrier electron and hole lifetimes in GaAs grown on metamorphic SiGe substrates," *Appl. Phys. Lett.*, vol. 84, 2004, pp. 3447.

[24] M. Y. Ghannam, et al., "Theoretical study of the impact of bulk and interface recombination on the performance of GaInP/GaAs/Ge triple junction tandem solar cells," in *Proc. 3rd World Conf Photovoltaic Energy Convers.*, 2003, pp. 666.

[25] J. A. Carlin, et al., "High-lifetime GaAs on Si using GeSi buffers and its potential for space photovoltaics," *Solar Energy Mater. Solar Cells*, vol. 66, 2001, pp. 621.

[26] S. M. Vernon, et al., "Experimental study of solar cell performance versus dislocation density," *in Proc. 21st IEEE Photovoltaic Spec. Conf.*, 1990, pp. 211.

[27] M. Yamaguchi, et al., "Effect of dislocations on the efficiency of thin-film GaAs solar-cells on Si substrates," *J. Appl. Phys.*, vol. 59, 1986, pp. 1751.

[28] M. Yamaguchi, et al., "Numerical-Analysis for high-efficiency GaAs solar-cells fabricated on Si substrate," *J. Appl. Phys*., vol. 66, 1989, pp. 915.

[29] C. L. Andre, et al., "Impact of dislocation densities on n(+)/p and p(+)/n junction GaAs diodes and solar cells on SiGe virtual substrates," *J. Appl. Phys.*, vol. 98, 2005, pp. 014502-1.

[30] J. C. Zolper and A. M. Barnett, "The effect of dislocations on the open-circuit voltage of gallium-arsenide solar-cells," *IEEE Trans. Electron Devices*, vol. 37, 1990, pp. 478.

[31] M.R. Lueck, et al., "Dual junction GaInP/GaAs solar cells grown on metamorphic SiGe/Si substrates with high open circuit voltage," *IEEE Electron Device Letters*, vol.27, 2006, pp. 142.

CHAPTER 2

[1] National Renewable Energy Laboratory Website - http://rredc.nrel.gov/solar/spectra/am1.5/

[2] Website: http://www.greenrhinoenergy.com/solar/radiation/spectra.php

[3] M.A. Green, "*Solar Cells: Operating principles, technology, and system applications*", New Jersey: Prentice Hall 1982.

CHAPTER 3

[1] Z. Q. Li, et al., and "2D-simulation of inverted metamorphic GaInP/GaAs/GaInAs triple junction solar cell," *in Proc. 33rd IEEE Photovoltaic Spec. Conf*., 2008, pp. 1.

[2] "APSYS, Advanced Physical Models of Semiconductor Devices" by Crosslight Software Inc., Burnaby, BC, Canada, ed.

[3] M. Yamaguchi, et al., "Numerical-Analysis for high-efficiency GaAs solar-cells fabricated on Si substrate," *J. Appl. Phys*., vol. 66, 1989, pp. 915.

[4] M. Yamaguchi and C. Amano, "Efficiency calcuations of thin-film GaAs solar-cells on Si substrates," *J. Appl. Phys*., vol. 58, 1985, pp. 3601.

[5] C. L. Andre, et al., "Impact of dislocations on minority carrier electron and hole lifetimes in GaAs grown on metamorphic SiGe substrates," *Appl. Phys. Lett*., vol. 84, 2004, pp. 3447.

[6] M. J. Yang, et al., "Photoluminescence analysis of InGaP top cells for high-efficiency multi-junction solar cells," *Solar Energy Mater. Solar Cells*, vol. 45, 1997, pp. 331.

[7] M. L. Lovejoy, et al., "Minority hole mobility in GaAs," in M.R. Brozel and G.E. Stillman (eds.), *Properties of Gallium Arsenide, Data Review Series no. 16*, London: INSPEC, 1996, pp. 123.

[8] R.K. Ahrenkiel and M. S. Lundstrom, "Minority carrier transport in III-V semiconductors," in R.K. Willardson, A.C. Beer, and E.R. Weber (eds.), *Minority Carrier in III-V*

Semiconductors: Physics and Applications, Semiconductors and Semimetals, vol. 39: Academic Press Inc., 1993, pp.193-258.

[9] M. Y. Ghannam, et al., "Theoretical study of the impact of bulk and interface recombination on the performance of GaInP/GaAs/Ge triple junction tandem solar cells," in *Proc. 3rd World Conf Photovoltaic Energy Convers*., 2003, pp. 666.

[10] T. Takamoto, et al., "Radiation resistance of high-efficiency InGaP GaAs tandem solar cells," *Solar Energy Mater. Solar Cells*, vol. 58, 1999, pp. 265.

[11] T. Takamoto, et al., "Structural optimzation for single junction InGaP solar cell," *Solar Energy Mater. Solar Cells*, vol. 35, 1994, pp. 25.

[12] I. Garcia, et al., "A 32.6% efficient lattice-matched dual-junction solar cell working at 1000 suns," *Applied Physics Letters*, vol. 94,2009, pp. 053509-3.

[13] T. Takamoto, et al., "Over 30% efficient InGaP/GaAs tandem solar cells," *Appl. Phys. Lett*., vol. 70, 1997, pp. 381.

[14] C. Algora, *et al.*, "Lattice-Matched III--V Dual-Junction Solar Cells for Concentrations Around 1000 Suns," *J. Sol Energ* , vol. 129, 2007, pp. 336.

CHAPTER 4

[1] Y. Takano, et al., "Reduction of threading dislocations by InGaAs interlayer in GaAs layers grown on Si substrates, "*Appl. Phys. Lett.* , vol. 73, 1998 pp. 2917.

[2] J. F. Geisz, et al., "High-efficiency GaInP/GaAs/InGaAs triple-junction solar cells grown inverted with a metamorphic bottom junction," *Appl. Phys. Lett*., vol. 91, 2007, pp. 023502-1.

[3] C. L. Andre, et al., "Impact of dislocations on minority carrier electron and hole lifetimes in GaAs grown on metamorphic SiGe substrates," *Appl. Phys. Lett*., vol. 84, 2004, pp. 3447.

[4] M. A. Green, et al., "Solar cell efficiency tables (version 41)," *Progress in Photovoltaics: Research and Applications*, vol. 21, 2013, pp. 1.

[5] W. Guter, et al., "Current-matched triple-junction solar cell reaching 41.1% conversion efficiency under concentrated sunlight," *Appl. Phys. Lett*., vol. 94, 2009, pp. 223504-1.

[6] S. R. Kurtz, et al., "Modeling of two-junction, series-connected tandems solar cells using top-cell thickness as an adjustable parameter," *J. Appl. Phys*., vol. 68, 1990, pp. 1890.

[7] M. Y. Ghannam, et al., "Theoretical study of the impact of bulk and interface recombination on the performance of GaInP/GaAs/Ge triple junction tandem solar cells," in *Proc. 3rd World Conf Photovoltaic Energy Convers*., 2003, pp. 666.

[8] N. Jain and M.K. Hudait, "Impact of Threading Dislocations on the Design of GaAs and InGaP/GaAs Solar Cells on Si Using Finite Element Analysis, " *IEEE Journal of Photovoltaics*, vol. 3, 2013, pp. 528.

[9] N. Jain and M.K. Hudait, "Design of metamorphic dual-junction InGaP/GaAs solar cell on Si with efficiency greater than 29% using finite element analysis," in *Proc. 38th IEEE Photovoltaic Spec. Conf*., 2012, pp. 002056.

CHAPTER 5

[1] D. Shahrjerdi, et al., "High-efficiency thin-film InGaP/InGaAs/Ge tandem solar cells enabled by controlled spalling technology," *Applied Physics Letters*, vol. 100, 2012, pp. 53901.

[2] B. Furman, et al., "A high concentration photovoltaic module utilizing micro-transfer printing and surface mount technology," in *Proc. 35th IEEE Photovoltaic Specialists Conference*, 2010, p. 475.

[3] R. Tatavarti, et al., "InGaP/GaAs/InGaAs inverted metamorphic (IMM) solar cells on 4" epitaxial lifted off (ELO) wafers, " in *Proc. 35th IEEE Photovoltaic Spec. Conf*, 2010, pp. 2125.

[4] Kayes BM, et al., "27.6% conversion efficiency, a new record for single-junction solar cells under 1 sun illumination," in *Proc. 37th IEEE Photovoltaic Spec. Conf.*, 2011, pp. 000004.

[5] V. Sabnis, et al., "High-efficiency multijunction solar cells employing dilute nitrides," *AIP Conference Proceedings*, vol. 1477, 2012, pp. 14.

[6] J. F. Geisz, et al., "High-efficiency GaInP/GaAs/InGaAs triple-junction solar cells grown inverted with a metamorphic bottom junction," *Appl. Phys. Lett.*, vol. 91, 2007, pp. 023502-1.

[7] S. M. Vernon, et al., "High-efficiency concentrator cells from GaAs on Si," in *Proc. 22nd IEEE Photovoltaic Spec. Conf*, 1991, pp. 353.